

1 **Inflammatory and regenerative processes in bioresorbable synthetic**
2 **pulmonary valves up to 2 years in sheep: Spatiotemporal insights**
3 **augmented by Raman microspectroscopy**

4

5 De Kort B.J.^{a,b}, Marzi J.^{c,d,e}, Brauchle E.^{c,d,e}, Lichauco A.M.^{a,b}, Bauer H.S.^f, Serrero A.^f,
6 Dekker S.^{a,b}, Cox M.A.J.^f, Schoen F.J.^g, Schenke-Layland K.^{c,d,e,h}, Bouten C.V.C.^{a,b}, Smits
7 A.I.P.M.^{a,b}*

8

- 9 a. Department of Biomedical Engineering, Eindhoven University of Technology,
10 Eindhoven, The Netherlands
- 11 b. Institute for Complex Molecular Systems (ICMS), Eindhoven University of Technology,
12 Eindhoven, The Netherlands
- 13 c. Department of Women's Health, Research Institute of Women's Health, Eberhard
14 Karls University Tübingen, Tübingen, Germany
- 15 d. NMI Natural and Medical Sciences Institute at the University of Tübingen, Reutlingen,
16 Germany
- 17 e. Cluster of Excellence iFIT (EXC 2180) "Image-Guided and Functionally Instructed
18 Tumor Therapies", Eberhard Karls University Tübingen, Tübingen, Germany
- 19 f. Xeltis B.V., Eindhoven, The Netherlands
- 20 g. Department of Pathology, Brigham and Women's Hospital, Harvard Medical School,
21 Boston, MA, USA
- 22 h. Department of Medicine/Cardiology, Cardiovascular Research Laboratories, David
23 Geffen School of Medicine at UCLA, Los Angeles, CA, USA

24 *Corresponding author: Dr.ir. A.I.P.M. (Anthal) Smits; a.i.p.m.smits@tue.nl Adress:
25 Eindhoven University of Technology, Department of Biomedical Engineering, P.O. Box
26 513; 5600 MB Eindhoven

27 **Abstract**

28 *In situ* heart valve tissue engineering is an emerging approach in which resorbable, off-
29 the-shelf available scaffolds are used to induce endogenous heart valve restoration. Such
30 scaffolds are designed to recruit endogenous cells *in vivo*, which subsequently resorb
31 polymer and produce and remodel new valvular tissue *in situ*. Recently, preclinical studies
32 using electrospun supramolecular elastomeric valvular grafts have shown that this
33 approach enables *in situ* regeneration of pulmonary valves with long-term functionality *in*
34 *vivo*. However, the evolution and mechanisms of inflammation, polymer absorption and
35 tissue regeneration are largely unknown, and adverse valve remodeling and intra- and
36 inter-valvular variability have been reported. Therefore, the goal of the present study was
37 to gain a mechanistic understanding of the *in vivo* regenerative processes by combining
38 routine histology and immunohistochemistry, using a comprehensive sheep-specific
39 antibody panel, with Raman microspectroscopy for the spatiotemporal analysis of *in situ*
40 tissue-engineered pulmonary valves with follow-up to 24 months from a previous
41 preclinical study in sheep. The analyses revealed a strong spatial heterogeneity in the
42 influx of inflammatory cells, graft resorption, and foreign body giant cells. Collagen
43 maturation occurred predominantly between 6 and 12 months after implantation, which
44 was accompanied by a progressive switch to a more quiescent phenotype of infiltrating
45 cells with properties of valvular interstitial cells. Variability among specimens in the extent
46 of tissue remodeling was observed for follow-up times after 6 months. Taken together,
47 these findings advance the understanding of key events and mechanisms in material-
48 driven *in situ* heart valve tissue engineering.

49

50 **Keywords:** Tissue-engineered heart valve (TEHV), *in situ* tissue engineering,
51 endogenous tissue restoration, biomaterial, foreign body response

52

53 **Introduction**

54 Surgical or interventional valve replacement is the standard of care treatment for most
55 patients with severe symptomatic valvular heart disease, and this treatment improves
56 quality of life and prolongs survival. Surgical valve replacement with either mechanical or
57 tissue valve substitutes (the latter composed of animal or human tissue and thus often
58 called bioprostheses) generally yield favorable long-term outcomes; survival is 50-70% at
59 10-15 years following valve replacement [1]. Nevertheless, valve-related problems
60 necessitate reoperation or cause death in more than half of patients with substitute valves
61 within 10-15 years postoperatively [2], [3]. Mechanical valves induce platelet deposition
62 and blood coagulation, (i.e., thrombosis) necessitating lifelong anticoagulation to reduce
63 the risk of prosthetic valve-related blood clots in patients receiving them. In contrast,
64 bioprostheses have low potential for thrombosis. However, despite improvements in
65 tissue treatments intended to enhance durability, bioprostheses frequently suffer structural
66 valve degeneration, often resulting from calcification, which is particularly accelerated in
67 children and young adults [4]. Although transcatheter valve replacement technologies
68 have recently gained favor, owing to less invasive implantation and good short-term
69 results, their long-term durability is uncertain [5], [6]. Recently the principle of *in situ* tissue
70 engineering (TE), also known as endogenous tissue restoration (ETR), has emerged as a
71 promising alternative [7]–[9]. This approach utilizes the regenerative capacity of the
72 human body to transform a resorbable polymeric implant into a living functional valve,
73 directly in its functional site, or *in situ*. The resorbable graft functions as a suitable valve
74 immediately upon implantation, and subsequently serves as an instructive template for
75 progressive endogenous cell infiltration and tissue deposition [7], [10].

76 Preclinical studies demonstrate the potential of *in situ* heart valve TE for pulmonary and
77 aortic valve replacements using varying materials, such as decellularized xeno- and
78 allogenic matrix (e.g. small intestine submucosa, SIS) [11]–[13], *in vitro* cultured and
79 decellularized matrices [14]–[17], and synthetic degradable polymers [18]–[21]. Promising

80 functionality has been reported, as well as successful *in situ* restoration processes,
81 including rapid cellularization, collagen deposition, endothelialization and material
82 resorption. Recently, the first report on ongoing clinical trials using resorbable
83 supramolecular elastomeric valves has been published, showing highly promising results
84 when applied as pulmonary valved conduits for right ventricular outflow tract
85 reconstruction in pediatric patients [22]. However, the regulation of the regenerative
86 response in the complex *in vivo* environment remains poorly understood [23], and
87 unexplained and uncontrolled adverse remodeling events such as loss of valve function,
88 due to valve thickening and shortening, have been reported in preclinical studies
89 (reviewed in [9]). Additionally, heterogeneity in remodeling processes, such as cell
90 infiltration, graft resorption and ECM deposition, has been reported between valves, as
91 well as between leaflets within the same valve [24], [25]. These variabilities in outcome
92 emphasize the need for more in-depth knowledge of the events, kinetics and mechanisms
93 involved in *in situ* TE, in order to achieve effective tissue formation, limit the risk of
94 unpredicted (maladaptive) remodeling and ensure safe clinical translation.

95 The goal of this study was to map the long-term spatiotemporal processes of polymeric
96 graft resorption, scaffold-induced inflammation and tissue regeneration in resorbable
97 synthetic pulmonary valves in sheep. To that end, in depth retrospective analysis was
98 performed on explant material of a previously reported preclinical study [19]. In that study,
99 supramolecular elastomeric heart valve grafts (Xeltis Pulmonary Valved Conduits, XPV,
100 Xeltis, Eindhoven, Netherlands) were implanted at the pulmonary position in an ovine
101 model with follow-up time up to 24 months. It was demonstrated that with this graft design,
102 safety and functionality remained acceptable throughout the follow-up time, and clinical
103 health, blood values and systemic toxicity were not influenced by the device. Gross
104 morphological analysis showed generally pliable leaflets, with some local anomalies, such
105 as focal leaflet thickening or rolling of the free edge of the leaflet. The grafts were
106 populated by endogenous cells from 2 months on, in both the conduit and the leaflet of the
107 valves. In order to advance the understanding of how recruited cells and cellular

108 interactions guide scaffold resorption and tissue formation *in vivo*, in the present study,
109 grafts from the previous *in vivo* study were analyzed using a comprehensive
110 immunohistochemistry (IHC) antibody panel [26] and Raman microspectroscopy [27][28].

111 The antibody panel for IHC was previously developed and validated and consists of
112 antibodies to mark inflammatory cells, valvular interstitial cells (VICs), and extracellular
113 matrix components, such as proteoglycans, collagens and elastic fiber-associated
114 proteins [26]. Specifically, we assessed the presence and phenotype of inflammatory and
115 VIC-like cells, paracrine signaling factors, endothelialization and microvascularization, and
116 extracellular matrix components related to collagen and elastin deposition.
117 Complementary to that, Raman microspectroscopy was applied to measure the local
118 molecular composition of graft material and newly formed tissue in various locations of
119 longitudinal sections of the explanted valves. Spectroscopic techniques are relatively
120 simple, reproducible and nondestructive. Raman microspectroscopy is a vibrational
121 spectroscopic technique that probes a specific chemical bond (or a single functional
122 group), yielding molecular-level information of functional groups, bonding types, and
123 molecular conformation, thus providing specific information about biochemical
124 composition of tissue constituents and their microenvironments [29], [30]. Specifically, we
125 applied Raman microspectroscopy on longitudinal sections of the valve explants including
126 conduit and leaflet to assess the local chemical changes in the scaffold materials,
127 indicative of scaffold resorption, as well as the composition and maturation of collagen in
128 different regions of interest of the valved conduit and for various follow-up times (2, 6, 12,
129 and 24 months). The measured trends on the molecular level were correlated to events on
130 the cell and tissue level using IHC analysis, providing new insights into the spatiotemporal
131 events of inflammation, tissue formation and maturation, and scaffold resorption during
132 material-driven *in situ* heart valve tissue engineering.

133

134 **Materials and methods**

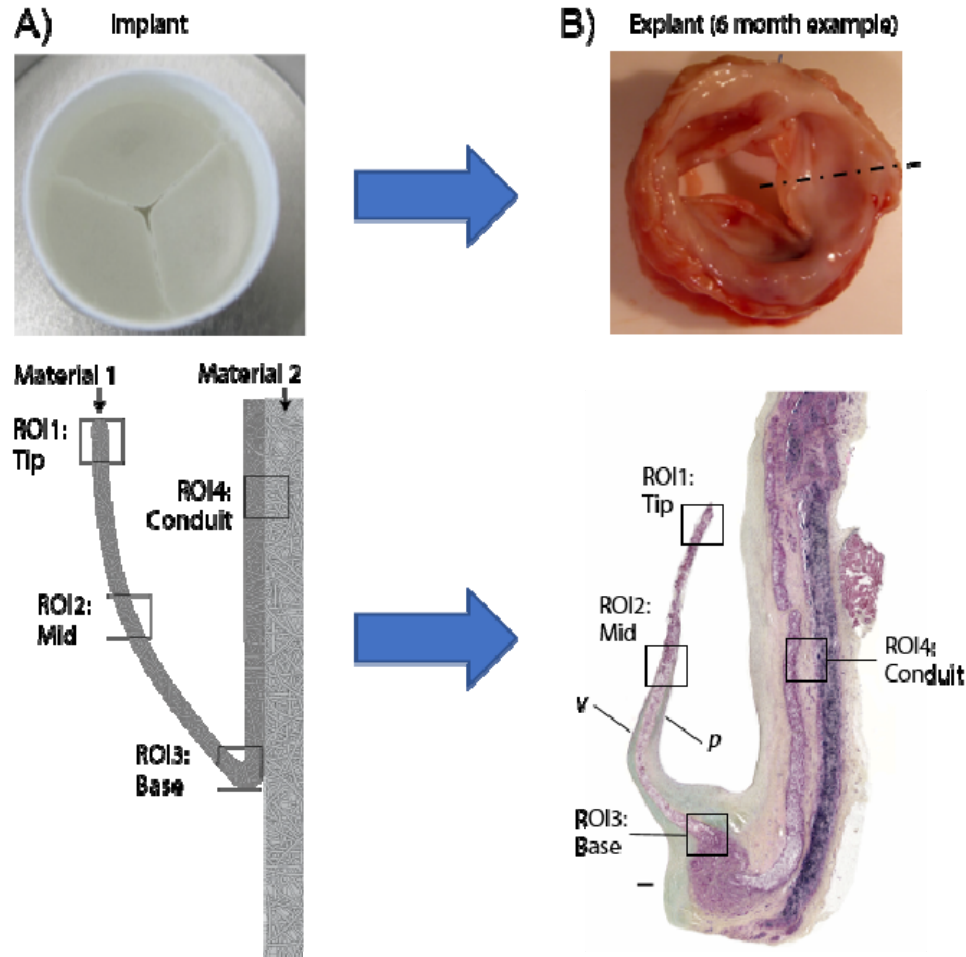
135 ***In vivo* study**

136 Explant material originates from a previously performed study (for detailed study design
137 [19]). Briefly, a valved conduit was produced from polycaprolactone-based supramolecular
138 polymer (electrospun polycaprolactone-ureidopyrimidinone; ePCL-UPy), material 1, and
139 polycarbonate-based supramolecular polymer (electrospun polycarbonate-
140 ureidopyrimidinone; ePC-UPy), material 2 (**Figure 1A**). Material 2 was designed to be
141 more stiff when compared to material 1 to provide robustness to the conduit, while
142 material 1 was designed to be more flexible and absorb more slowly, to accommodate the
143 mechanical requirements as well as an anticipated slower restoration process for the
144 leaflets. The conduits were implanted in the pulmonary position in adult Swifter sheep
145 (age 2-4 years, weight 60-90kg) and the valves were explanted for analysis after 2 months
146 (N=5), 6 months (N=5), 12 months (N=5), and 24 months (N=2) *in vivo*. The animal usage
147 and study design were approved by the Test Facility's Ethical Committee (Medanex
148 Belgium) for compliance with regulations and the Helsinki protocol. Furthermore, animal
149 welfare was in compliance with the Directive 2010/63/ EU.

150 **Tissue preparation**

151 The right ventricular outflow tract including the pulmonary valve was excised and fixed in
152 4% neutral buffered formalin solution. The conduit was opened longitudinally and
153 transmural specimens incorporating the leaflets and conduit wall were used for further
154 analysis (**Figure 1B**). The specimens were dehydrated, embedded in paraffin, and
155 sectioned at 4 to 6 microns. Sections were de-paraffinized by washing 3 times 10 minutes
156 with xylene and rehydrated using a decreasing alcohol series. Subsequently, the sections
157 were washed with deionized water and afterwards phosphate buffered saline (PBS, pH
158 7.4, Sigma).

159



160

161 **Figure 1: Overview of valve composition at implantation and explantation.** A) Top view of the
162 electrospun valved conduit with schematic longitudinal cross-section, indicating the composite
163 design with material 1 (conduit + leaflet) and material 2 (conduit only), and regions of interest
164 (ROIs) for analysis as indicated. B) Representative example of an explanted valve (6-month
165 example) with gross morphological photograph, indicating cutting plane through the center of the
166 leaflet, resulting in a longitudinal section through both the leaflet and conduit. Displayed is a Movat
167 Pentachrome staining with ROIs for analysis as indicated. P and v indicate the pulmonary and
168 ventricular surfaces of the leaflet, respectively. Photographs and Movat Pentachrome staining are
169 adapted from[19].

170

171 **Immunohistochemistry**

172 IHC was performed to evaluate the presence and phenotype of infiltrating inflammatory
173 cells (inducible nitric oxide synthase, iNOS; CD64; CD163; CD44), VIC-like cells (α -
174 smooth muscle actin, α SMA; embryonic form of smooth muscle myosin heavy chain,
175 SMemb; vimentin; calponin), paracrine signaling factors (tumor necrosis factor- α , TNF- α ;
176 interleukin-10, IL-10; transforming growth factor- β_1 , TGF- β_1), endothelial cells (von
177 Willebrand Factor, vWF), and extracellular matrix components (collagen 1, collagen 3,
178 (tropo)elastin, fibrillin-1, fibrillin-2) (**Supplementary Table 1**). Antibodies were selected
179 from a previously developed sheep-specific panel [26] and performed on all explant
180 tissues as described. The dilutions and antigen retrieval methods per antibody are
181 specified in **Supplementary Table S1** and detailed staining protocol is specified in the
182 **Supplementary Methods**. Briefly, biotin-labeled secondary antibodies were used and
183 after staining, slides were either treated with SIGMA FAST™ BCIP/NBT (5-Bromo-4-
184 chloro-3-indolulphosphate/Nitro blue tetrazolium, pH 9.5, Sigma) and counterstained with
185 nuclear fast red (Sigma) or treated with LSAB Streptavidin and Nova Red chromogen and
186 counterstained in Hematoxylin. For each stain, an appropriate negative and positive
187 control tissue was selected and included, being either ovine spleen or aortic valve tissue.
188 After dehydration and coverslipping, the stained sections were digitally scanned by
189 CVPPath at 20X magnification (CVPPath institute Inc, Gaithersburg, US).

190 **Semi-quantitative analysis of stainings**

191 Semi-quantitative analysis was performed for specified regions of interest (ROIs), i.e.
192 within the graft material of the tip (ROI1) , mid (ROI2) and base (ROI3) of the leaflet, the
193 conduit (ROI4) of the pulmonary artery (**Figure 1A, B**), and the neotissue deposition onto
194 the pulmonary artery. For each stained section, images (1.000.000 μm^2) were selected for
195 the ROI, as well as an image for counterstain reference and background reference using
196 digital analysis software (QuPath) [31]. The ROIs were exported to ImageJ software (NIH,
197 Bethesda, MD, USA) which counted pixel intensities and converted these to a histogram.

198 Based on the intensity of the background and counterstain reference, thresholds were set
199 in order to determine the ranges for positive staining intensity and counterstain intensity.
200 The percentage of positive pixels was then determined by dividing the number of pixels in
201 the positive expression range by the number of pixels in the positive and counterstain
202 region, therefore, excluding background signal and graft material. Data were expressed as
203 boxplots including individual data points using Prism software 5.0 (GraphPad Software, La
204 Jolla, CA). A detailed protocol for the semi-quantitative analysis is specified in the
205 **Supplementary methods.**

206 **Raman Microspectroscopy**

207 Raman images were acquired from de-paraffinized and rehydrated tissue sections using a
208 Raman microspectroscope (alpha300 R WITec, Ulm Germany). Samples were excited
209 using a 532 nm laser and output laser power was 60 mW. Areas of 500 x 500 μm were
210 scanned in the following regions of interest: tip (ROI1), mid (ROI2) and base of the leaflet
211 (ROI3) and the material interface in the conduit (ROI4) (**Figure 1A, B**). The spectral maps
212 were collected using a line scanning mode (250 lines, 250 points/line, spectral acquisition
213 time=0.05 s/pixel), creating a pixel size of 2 x 2 μm .

214 **True Component Analysis and Principal Component Analysis of Raman spectra**

215 Raman spectra represent a highly specific fingerprint, providing molecular information on
216 a sample [32], [33]. Multivariate data analysis tools are needed to access the
217 comprehensive information provided by the spectral features and to generate false color-
218 coded intensity distribution heatmaps from hyperspectral imaging maps. Here, we
219 performed True Component Analysis (TCA) to map the location of scaffold components
220 and biological tissue components in each sample. These components were then further
221 analyzed for their molecular composition using Principal Component Analysis (PCA).
222 Specifically, the scaffold material components as identified with TCA were analyzed for
223 chemical changes indicative of scaffold resorption and the biological tissue components
224 were analyzed for collagen formation and maturation.

225 Image-based data analysis was performed using Project Five Plus Software (WITec, Ulm,
226 Germany). Of each image, data sets were pre-processed using cosmic ray removal and
227 shape background correction. The spectra were cropped (spectral range of 250-3050 cm⁻¹)
228 ¹) and normalized to the area of 1. Reference spectra were measured of both non-
229 implanted graft materials (Xeltis) and biological components, including fibrin (human
230 plasma, sigma Aldrich #F5386), collagen 1 (lyophilized collagen 1 from porcine skin, EPC-
231 elastin products, USA), erythrocytes, and blood components (the latter both extracted
232 from the explant images itself). All Raman images were analyzed using TCA to identify
233 known biological and graft material components in the recorded explant spectra based on
234 the reference spectra (**Supplementary Figure S1**). The pixels that were recognized as
235 similar spectra were assigned to the same spectral component and visualized as intensity
236 distribution heatmaps to localize the different molecular components. Additionally, single
237 point spectra of material and collagen components were extracted and analyzed using
238 principle component analysis (PCA) using Unscrambler X14.2 (Camo, Software, Norway)
239 to investigate molecular differences between the ROIs and between timepoints. The PCA
240 algorithm (NIPALS) allows to decompose the spectral information deciphering spectral
241 similarities and differences into defined vectors – so called principal components (PC).
242 Thereby, PC-1 explains the most influencing spectral signatures, PC-2 the second most
243 relevant information and so on. The PC scores plot can support the visualization of a
244 separation within the dataset. The underlying spectral information is indicated in the
245 corresponding PC loadings plot identifying bands assigned to positive score values as
246 positive peaks and Raman shifts dominating in data with negative score values as
247 negative loadings peaks. PC scores plots and loadings plots were employed to visualize
248 differences of *in vivo* material and collagen spectra at different ROIs and timepoints.

249

250 **Results**

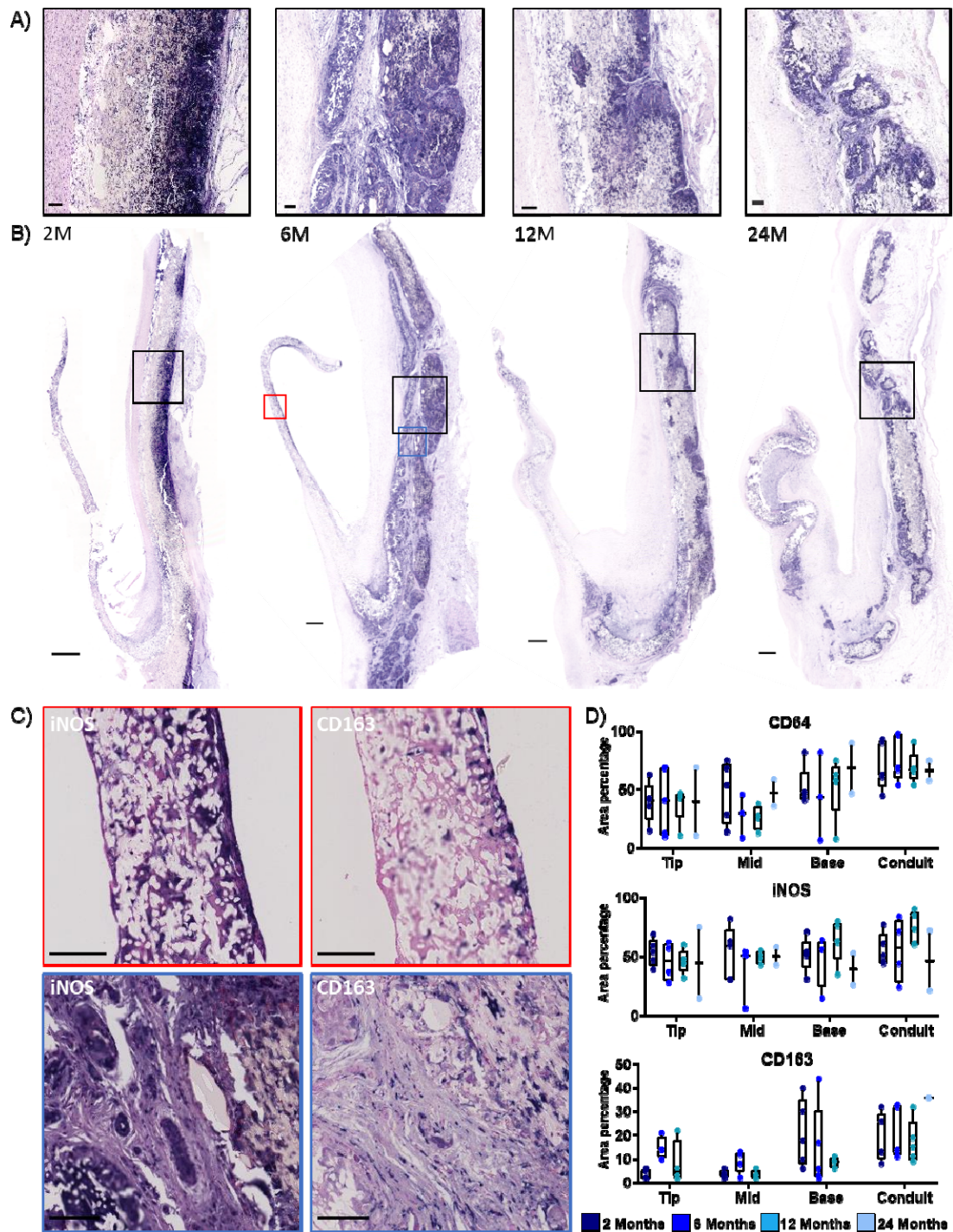
251 ***Spatial heterogeneity in inflammatory cell influx with mixed phenotypes***

252 The *in vivo* functionality and general morphological analysis of the valved conduits up to
253 12 months of implantation has previously been reported by Bennink et al. [19]. The
254 present study extends the depth of analysis of the specimens to yield a deeper
255 understanding of the processes involved.

256 To augment the conventional assessment by tissue morphology of the presence and
257 phenotype of infiltrating inflammatory cells, sections were stained by
258 immunohistochemical methods for the general macrophage marker CD64, as well as the
259 pro- and anti-inflammatory markers iNOS and CD163, respectively, complemented with
260 cytokine stainings for TNF- α , IL-10 and TGF- β_1 (**Figure 2**). CD64⁺ macrophages were
261 detected within the whole leaflet material, as well as the conduit. The distribution was
262 heterogeneous with most abundant presence in the base region of the leaflet and in
263 material 2 of the conduit wall, although the extend was variable between explants (**Figure**
264 **2A,B,D**). In the leaflet, less macrophages were detected in the mid region after 6 and 12
265 months when compared to the base and tip regions. However, an increase was seen in
266 the mid region at 24 months (**Figure 2D**). Over time, macrophages generally remained
267 present around and within remaining graft material, and macrophage presence diminished
268 with full graft resorption, as was seen for example in the base region of the leaflet after 24
269 months. Macrophages were mainly present within and close to the graft material, however
270 one 2 month explant was exceptional. Within the lumen of the neointima, erythrocyte-rich
271 matrix was present in which many macrophages resided, suggesting that the influx of
272 erythrocytes might be a cue for macrophage recruitment (**Supplementary Figure S2**).

273 In terms of macrophage polarization and general inflammatory state, a mixed
274 inflammatory profile of both pro-inflammatory and anti-inflammatory markers was detected
275 throughout the implantation time within the leaflet base and the conduit (**Figure 2 C,D**). At
276 the tip and mid regions of the leaflet, however, macrophages predominantly expressed

277 iNOS but not CD163 at the 2 month timepoint. After 6 months, anti-inflammatory marker
278 expression increased within the tip of the leaflet, whereas in the mid region this increase
279 was less abundant. Expression of TNF- α and IL-10 generally correlated with the presence
280 of iNOS⁺ pro- and CD163⁺ anti-inflammatory macrophages respectively. Additionally,
281 TGF- β_1 (**Supplementary Figure S3**) was mainly detected within graft material in regions
282 with ongoing inflammation.



283

284 **Figure 2: Macrophage infiltration and polarization over time is region specific.** A, B)
285 Representative images of 2, 6, 12, and 24 month explants stained for general macrophage marker
286 CD64, with whole-valve scan and higher magnification images of areas within the graft material of
287 the conduit (location indicated by black boxes) showing that CD64⁺ macrophages localized within
288 both leaflet and conduit graft material. Positive staining in purple, counterstain in pink. Scale bars,

289 500 μm for whole-valve scan, 100 μm for zooms. C) Representative images of the pro-
290 inflammatory marker inducible nitric oxide synthase (iNOS) and anti-inflammatory marker CD163 at
291 the mid region of the leaflet (red boxes) and the conduit (blue boxes) of a 6 month explant showing
292 mixed polarization with dominance of pro-inflammatory macrophages within the leaflet graft
293 material and increased anti-inflammatory marker expression within the conduit material. Scale bar,
294 100 μm . D) Semi-quantification of immunohistochemical stainings (area 100.000 μm^2). N=1 for
295 quantification of the 24 month CD163 staining due to processing artifacts in the CD163 staining of
296 one of the 24 month valves.

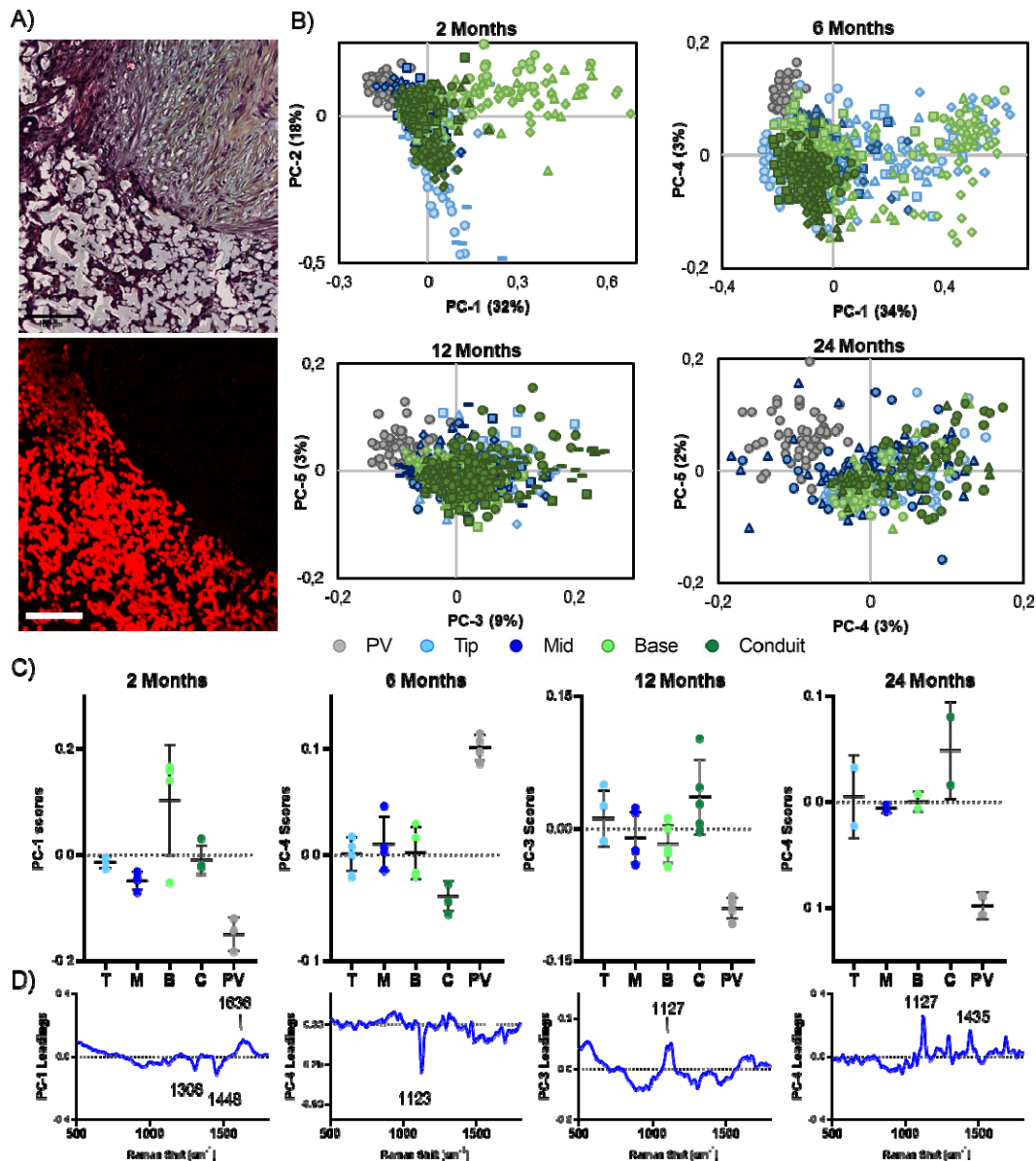
297 ***Regional heterogeneity in graft resorption correlates with foreign body giant cell*** 298 ***formation***

299 Having established the heterogenous influx of inflammatory cells in the conduit and leaflet
300 materials, we then analyzed the extent of graft resorption and tissue formation in the
301 different regions of the valve. To that end, Raman microspectroscopy was performed in
302 the specified regions of interest to acquire the molecular composition in each area. The
303 general local composition of scaffold materials and biological components was determined
304 via TCA. In order to analyze graft resorption per material, the spectra of material 1 and 2
305 were distinguished from the biological spectra using TCA (**Supplementary Figure S1**).

306 The spectra for material 1 and 2 were analyzed separately and compared to the pre-
307 implant composition of each material using PCA. For the scaffold materials components,
308 spectral changes were mainly dominated by an increasing 1123 cm^{-1} band with
309 implantation duration in both material 1 and 2. The molecular assignment of this band is
310 linked to C-O stretch vibrations and could be linked to an increasing contribution of alkyl-
311 hydroxy groups referring to a degradation of the polymer. The exterior region of the
312 conduit, consisting of material 2, demonstrated major molecular alterations as seen as an
313 increase in the 1123 cm^{-1} band already after 2 months, indicative of early resorption of
314 material 2, with more progressive resorption over time (**Supplementary Figure S4**). The
315 resorption of material 1 was analyzed per region of interest (**Figure 3**). Multivariate
316 analysis of the spectra extracted from the scaffold material maps (**Figure 3A, B**) and

317 comparison of the average score values for each animal (**Figure 3C**) demonstrated the
318 most significant variation in the spectral signature arising between non-implanted polymer
319 material and implanted grafts. Corresponding loadings plots depicted the most influencing
320 spectral features (**Figure 3D**). After 2 months, spectral differences were mainly assigned
321 to intensity differences of the overall polymer spectrum, indicating general erosion of the
322 material rather than molecular changes of the material. Resorption of material 1 after 2
323 months was most pronounced in the base of the leaflet. 6, 12 and 24 months samples
324 showed alterations in the chemical composition of the polymer with a major influence of
325 an increasing band at 1123 cm^{-1} indicating polymer resorption, which was most
326 pronounced in the conduit region. Most variability in chemical composition amongst
327 explants was present after 2 and 6 months of implantation.

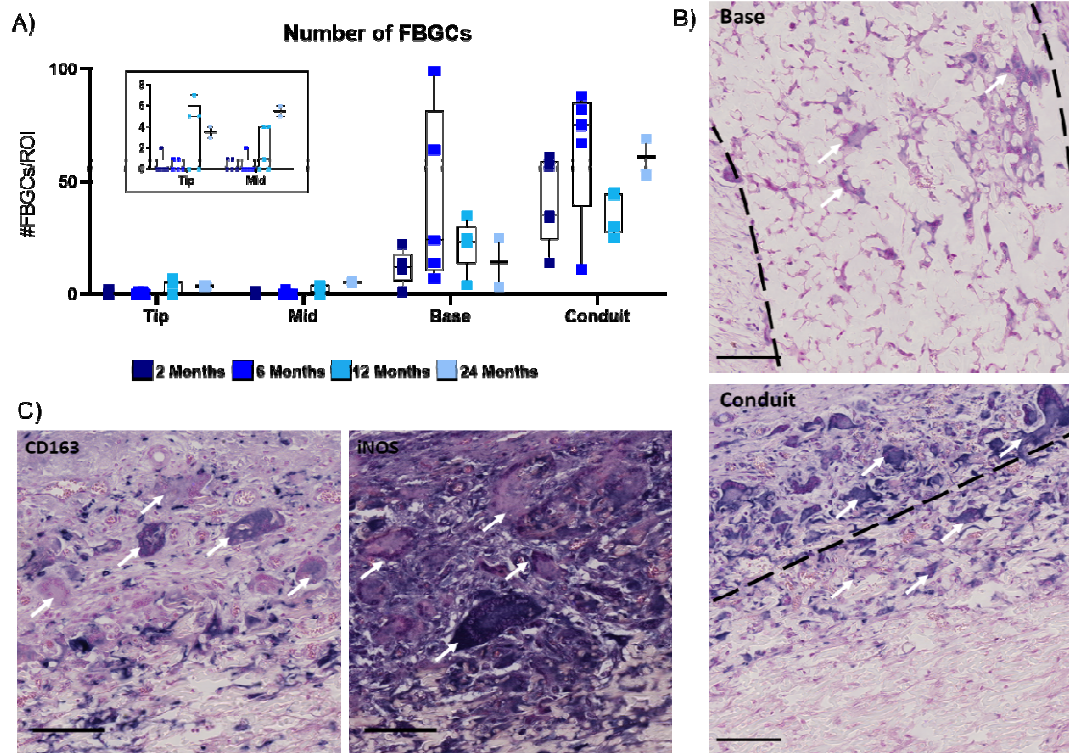
328 Within the identified areas with most pronounced graft resorption, foreign body giant cells
329 (FBGCs) were present in an inflammatory environment and remained present until full
330 graft resorption, implying a correlation between the presence of FBGCs and graft
331 resorption. In the conduit and leaflet base regions, FBGCs were present already after 2
332 months (**Figure 4A**). In the conduit, FBGCs formed predominantly at the outer boundaries
333 of the graft material, rather than inside the graft pores, encapsulating the graft material. In
334 the base region of the leaflet, on the other hand, FBGCs also formed within the pores of
335 the microfibrinous graft material (**Figure 4B**). Substantial variability in the overall number of
336 FBGCs was detected in the conduit and base regions, especially at 2 and 6 months
337 (**Figure 4A**). Few FBGCs were present in the tip and mid regions of the leaflet at all
338 timepoints, with a slight increase over time. Heterogenous expression of both pro- and
339 anti-inflammatory markers, iNOS and CD163 respectively, were present in FBGCs
340 (**Figure 4C**).



341

342 **Figure 3: Raman analysis of *in vivo* resorption of pulmonary valve implant material 1.** A)
 343 Movat Pentachrome stained base region of a 2 month explant and respective true component
 344 analysis (TCA) map of material 1 of this specific region (TCA component of material 1 depicted in
 345 red). B) Material 1 spectra were compared for different leaflet regions (ROI1-4) and non-implanted
 346 material (PV) after 2, 6, 12, and 24 months using principal component analysis (PCA) scores plot.
 347 For each PCA, spectra of the same valve are indicated with the same symbol shape. C)
 348 Comparison of ROI-specific average principal component (PC) score values (from B) for each
 349 timepoint indicated the biggest discrepancy between implanted and non-implanted material and a
 350 tendency towards the strongest resorption in the conduit region. D) Corresponding loadings plots

351 for PCs as indicated. After 2 months, mainly differences in overall polymer signature and intensity
352 were detected. The 6, 12 and 24 month timepoints highlighted a significant band at 1123/1127 cm^{-1}
353 increasing upon polymer resorption.



354

355 **Figure 4: Overview of foreign body giant cell (FBGC) formation over time.** A) FBGCs within
356 each ROI ($1,000,000 \mu\text{m}^2$) were counted in immunohistochemical images (from CD44 staining),
357 with highest presence in the leaflet base and conduit. B) FBGCs (CD44 staining, positive staining
358 in dark purple), indicated by arrows, within the micropores of the graft material of the base region
359 and the outer layer of the conduit material after 2 months of implantation. Dashed lines indicating
360 the tissue-graft interface. Scale bars, 100 μm . C) Heterogeneity between in pro- and anti-
361 inflammatory marker expression, iNOS and CD163 respectively, in formed FBGCs, indicated by
362 arrows, in the conduit of a 2 month explant. Positive staining in purple, counterstain in pink. Scale
363 bars, 100 μm .

364

365

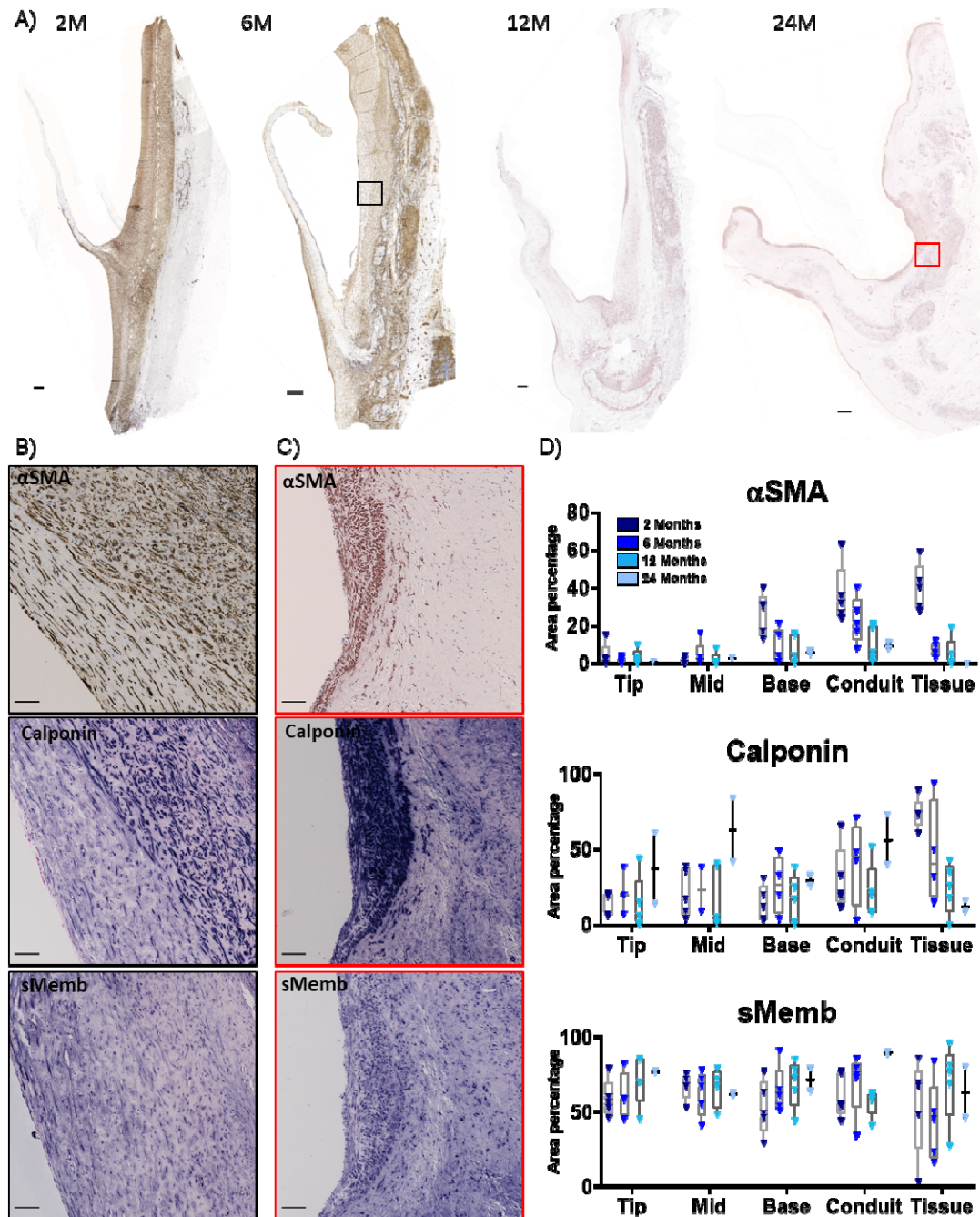
366 ***VICs transition towards a quiescent phenotype over time***

367 The presence and distribution of tissue producing cells was analyzed by
368 immunohistochemical stainings for α SMA, SMemb and calponin, representing markers for
369 (myo)fibroblast and VIC-like cell activation. At 2 months, many α SMA⁺, SMemb⁺, and
370 calponin⁺ cells were present within the layer of neotissue covering the graft materials, as
371 well as within the microporous graft material at the conduit and base regions specifically
372 (**Figure 5A,D**). At this time point, SMemb⁺ and calponin⁺ cells were also present within the
373 leaflet, whereas no α SMA⁺ cells were present in the leaflet. At 6 months, α SMA⁺ cells had
374 migrated towards the tip of the leaflet in most explants (**Figure 5A**). At 12 months, the
375 overall presence of VIC-like cells decreased, especially in the graft material and neotissue
376 of the conduit and base regions. Moreover, a strong decrease in overall α SMA expression
377 was observed between 6 and 12 months, indicative of a more quiescent VIC-like
378 phenotype (**Figure 5D**). However, SMemb expression remained high over time. Vimentin
379 and CD44 expression was minimal in all explant at all time points, with expression
380 restricted to FBGCs within the graft material (**Supplementary Figure S5**).

381 Heterogeneity in tissue deposition as well as presence and morphology of the VICs
382 between explants and the ROIs within one explant was seen (**Figure 5B, C**). The
383 morphology of cells varied between regions with different collagen expression, with
384 elongated cells detected in regions that were rich in fibrillar collagen 1, and rounded cells
385 in regions with more a dense, collagen 3-rich matrix (**Supplementary Figure S6**).
386 Biglycan and TGF- β_1 expression tended to correlate to calponin and α -SMA expression,
387 suggesting these cells to be predominant producers of these proteins (**Supplementary**
388 **Figure S6**).

389

390



391
392

Figure 5: Valvular interstitial cell (VIC) phenotype shifts towards quiescent state over time.

393 A) Overview of α -smooth muscle actin (α SMA) expression in representative explants at 2, 6, 12,
394 and 24 months. Over time, presence of α SMA⁺ cells decreased and remaining α SMA⁺ cell localized
395 close to endothelium. Positive staining in brown, nuclei in blue. Scale bars, 500 μ m. B) and C)
396 Heterogeneous α SMA, calponin and embryonic smooth muscle myosin heavy chain (sMemb)
397 expression in areas with neotissue deposition onto the conduit after 6 months (B) and 24 months
398 (C) of implantation. Locations indicated with black and red boxes in A. Calponin and sMemb;

399 positive staining in purple counterstain in pink. Scale bars, 100 μm . D) Semi-quantification of
400 αSMA , calponin and SMemb staining within the leaflet Tip, Mid and Base regions, in the Conduit
401 and in the layer of neotissue deposited onto the graft material in the conduit (Tissue).

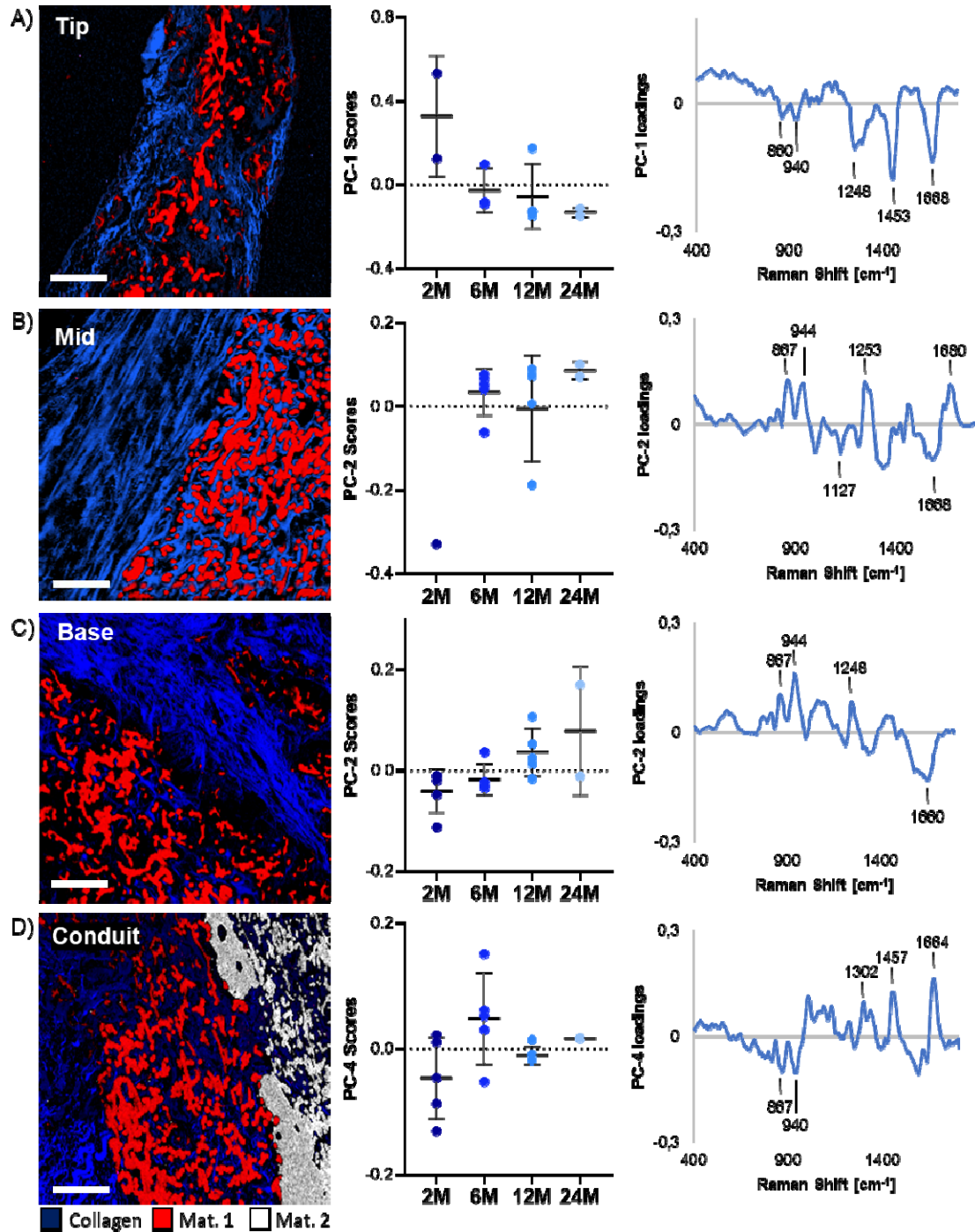
402

403 ***Collagen maturation between 6 and 12 months of implantation with limited*** 404 ***elastogenesis***

405 Having established the spatiotemporal patterns in the phenotype of tissue-producing cells,
406 we then assessed the composition and maturation of the endogenously produced tissue.
407 To that end, the fingerprint region of the biological component of the Raman spectra was
408 analyzed for collagen maturation, in combination with immunohistochemical analysis.
409 Overall, there was progressive tissue deposition in the TEHVs, in the form of pannus
410 formation on the blood-contacting surface of the graft material as well as tissue formation
411 in between the microporous graft fibers as seen in the TCA images (**Figure 6A,**
412 **Supplementary Figure S7**). PCA analysis of the Raman spectra in the tip and mid
413 regions of the leaflet revealed a predominant shift in PC scores between 2 and 6 months,
414 indicating that collagen deposition within the graft material in these regions was mostly
415 detected from 6 months on (**Figure 6A, B**). The loading plots revealed that changes over
416 time within the leaflet tip and mid regions were dominated by increasing peaks at 860, 940
417 and 1250 cm^{-1} assigned to the C-C collagen backbone as well as to hydroxyproline, which
418 are mainly linked to overall collagen content (**Figure 6A, B**). In contrast, the PC scores for
419 the leaflet base and conduit regions showed a more gradual shift between time points,
420 which indicates that collagen was already deposited at 2 months, followed by gradual
421 maturation over time (**Figure 6C, D**). In the leaflet base, implantation-time dependent
422 findings were observed, with an increasing influence of the amide I band around 1660 cm^{-1} ,
423 referring to 3D structural changes due to alterations of α -helix and β -sheet contribution
424 which are present in more stable collagen structures [34] (**Figure 6C**). The tissue within
425 the conduit indicated slightly different molecular alterations compared to the other regions,

426 with collagen signatures dominated by (hydroxy-)proline at early timepoints, whereas at
427 later timepoints signal intensities assigned to amide I (1664 cm^{-1}) and III (1250 cm^{-1}) as
428 well as the C-C backbone (1450 cm^{-1}) increased (**Figure 6D**).

429 To evaluate the extent of collagen maturation specifically, the high wavenumber regions of
430 Raman spectra were analyzed, as shown in **Supplemental Figure S8**. A strong shift in
431 the PC scores was detected between 6 and 12 months in the base and mid regions of the
432 leaflet, as well as the conduit. Peaks at 2855 , 2877 and 2955 cm^{-1} characteristic for
433 mature collagen type 1 [35] were strongest after 12 and 24 month of implantation in these
434 regions, indicating maturation occurred predominantly between 6 and 12 months. This
435 maturation was confirmed at the protein level by immunohistochemical stainings for
436 collagen type 1 and 3 (**Figure 7A,B**). Specifically, the immunohistochemical analysis
437 showed a gradual increase in collagen type 1 within the graft material over time (**Figure**
438 **7A**). In addition, a layer of collagenous neotissue was covering the graft material in the
439 conduit region, as well as the base and mid regions of the leaflet (**Figure 7B**). Tissue
440 deposition on the leaflet tended to occur predominantly on the ventricular side at early
441 time points, progressing from the base region to the mid region of the leaflet. The layers of
442 neotissue were rich in collagen 3 and low in collagen 1 after 2 months of implantation,
443 while over time, collagen 1 expression increased. This was accompanied by the formation
444 of more aligned, fibrous organization, indicating collagen maturation, particularly in the
445 neotissue covering the leaflet (**Figure 7B**). Within the graft material in the base region, the
446 collagen had a random orientation, while the neotissue at the conduit consisted of more
447 dense collagenous tissue, when compared to the leaflet (**Figure 7B**).



448

449

Figure 6: Raman microspectroscopic analysis of collagen maturation. True Component

450 Analysis (TCA) mapping shows the localization of spectra linked to collagen (blue), material 1 (red)

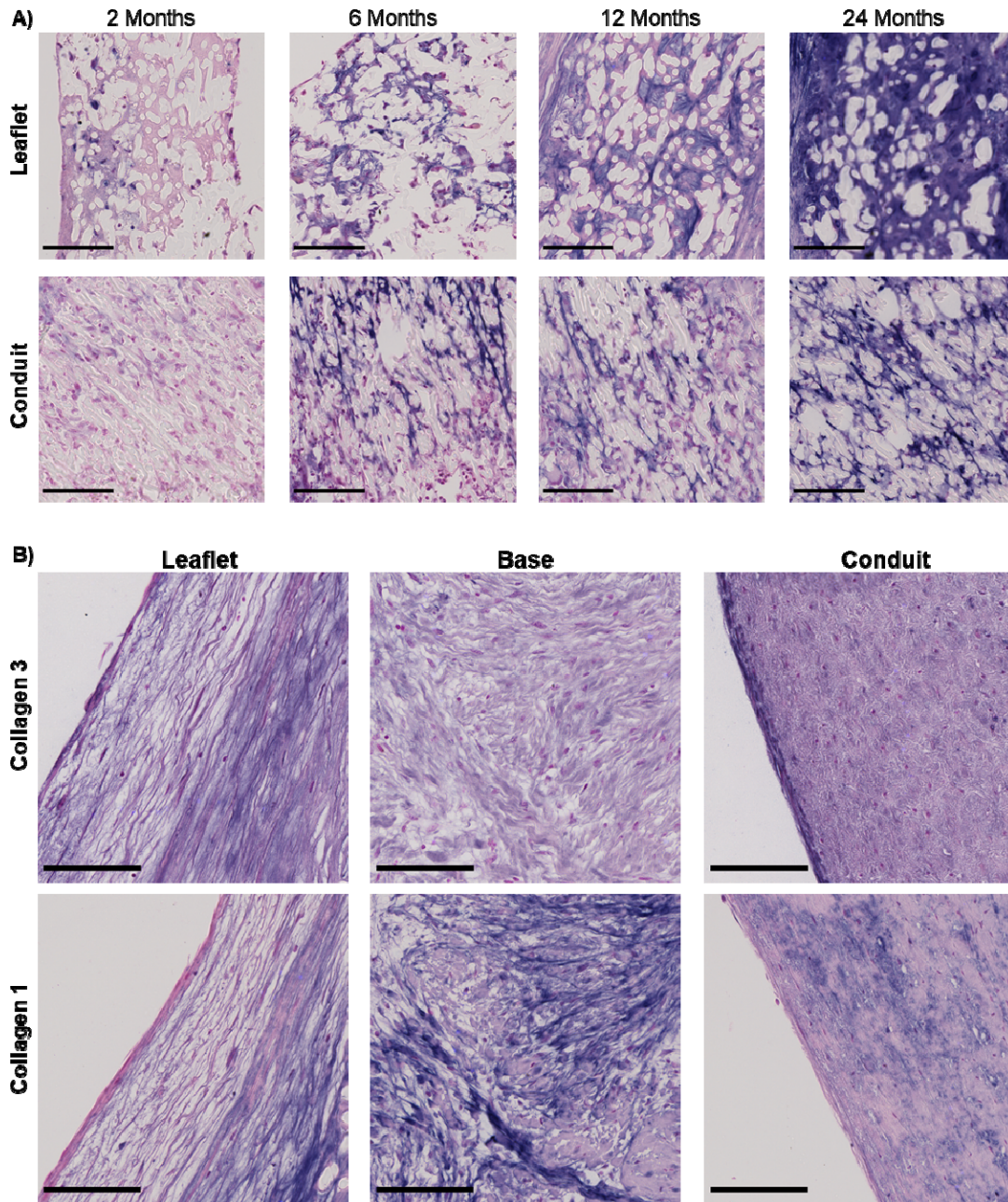
451 and material 2 (white) for the leaflet tip (A), mid (B), base (C) and conduit (D) regions. Principal

452 Component Analysis (PCA) was performed on the collagen component from the TCA to study

453 collagen maturation with time of implantation. Displayed are the Principal Component (PC) score

454 plots (middle column) and the corresponding loadings plots (right column) for each ROI.

455 Differences in leaflet tip and mid regions were mainly linked to the overall collagen content
456 indicated by bands at 860, 940 and 1250 cm^{-1} assigned to the C-C collagen backbone and
457 hydroxyproline. In the base and conduit additional structural changes related to shifts in the amide I
458 band (1660 cm^{-1}) were observed, indicating collagen maturation.

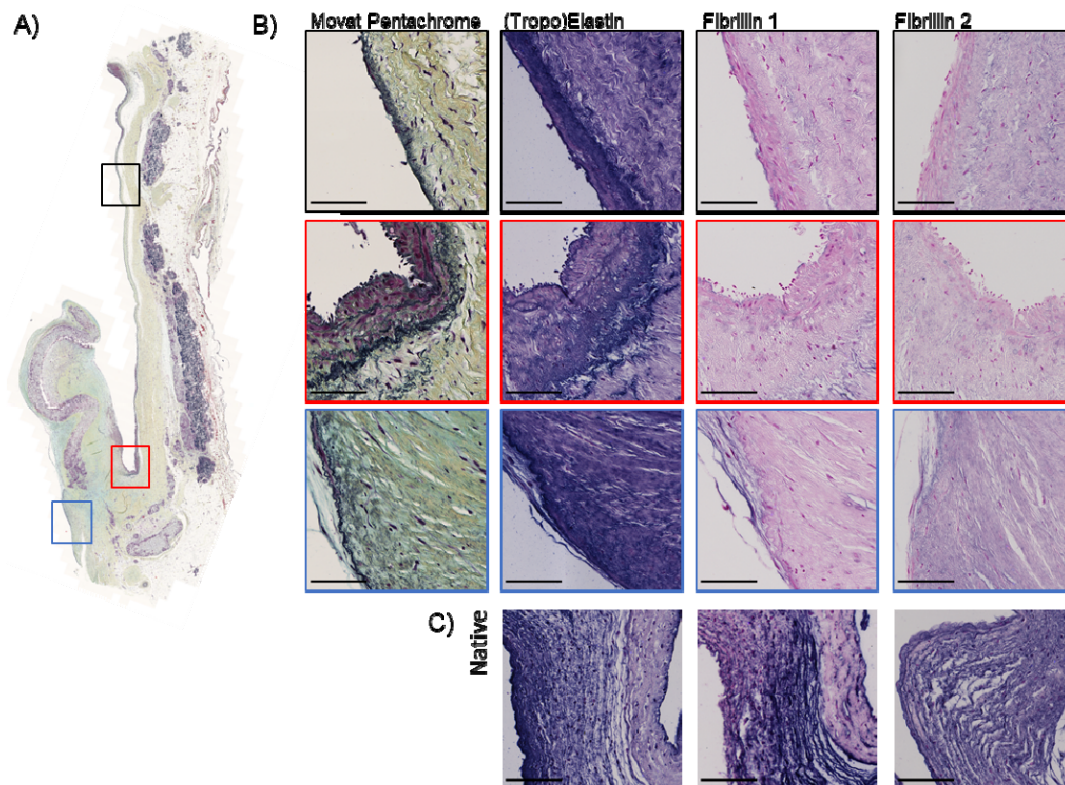


459
460 **Figure 7: Spatiotemporal heterogeneity in collagen deposition and maturation.** A)
461 Representative images of immunohistochemical staining of Collagen 1 within graft material of the
462 leaflet and conduit. Collagen 1 within the conduit material became more fibrillar over time
463 compared to the leaflet. Scale bars, 100 μm . B) Representative images of collagen 3 and collagen

464 1, showing variations in composition and organization of collagen in the neotissue of the leaflet,
465 base and conduit after 12 months of implantation. Scale bars, 100 μ m. For all images, positive
466 staining in dark purple, counterstain in pink.

467

468 In addition to collagen fibers, the endogenous formation of a mature elastic fiber network
469 in the valves was assessed. Premature elastic fibers were detected at 24 months, most
470 often located near the conduit region, as well as the leaflet base region, both at the
471 ventricular and pulmonary side (**Figure 8A**). In all explants, (tropo)elastin was highly
472 expressed within the layer of neotissue (**Figure 8B**). In some 6- and 12-month valves,
473 fibrillin 2 was expressed within these regions. However, (tropo)elastin expression
474 generally did not colocalize with the microfibrillar proteins fibrillin 1 or 2, both of which are
475 necessary to form mature elastic fibers, as also evident from control staining of native
476 sheep aortic valve tissue (**Figure 8C**).



477

478 **Figure 8: Elastic fiber network formation in 24-month explant.** A) Movat pentachrome staining
479 showing mature elastic fibers in black in a 24-month explant. Elastic fiber network formation mainly

480 occurred near the lumen of the base region (Red and Blue zooms) and conduit (Black zoom). B)
481 Antibody staining of the corresponding regions with (tropo)elastin, fibrillin 1 and fibrillin 2 (positive
482 staining in purple and counterstain in pink), indicating a high expression of (tropo)elastin, but
483 limited fibrillin 1 and fibrillin 2 expression. C) Positive control of the staining on native sheep aortic
484 valve. Scale bars, 100 μ m.

485

486 ***Endothelialization and microvascularization within the microporous graft material***

487 vWF staining was performed to study endothelialization and microvascularization. After 2
488 months, vWF expression was present at the luminal surface of the neotissue layer
489 deposited on the conduit, with higher expression on the proximal side of the valve
490 compared to the distal side (**Supplementary Figure S9**). Sparse expression was
491 detected at the surface of the neotissue layer formed at the base region of the leaflet,
492 predominantly at the pulmonary side and to lesser extent on the ventricular side. After 12
493 months, the endothelial layer was more pronounced, with expression of vWF on the
494 neotissue of the whole leaflet, on both the pulmonary and ventricular side.

495 Additionally, vWF was detected within and close to the material of the conduit at all time
496 points, indicating the formation of microvasculature within the microporous graft material
497 (**Supplementary Figure S10**). In the leaflet, no microvessels were detected within the 2-
498 and 6-months explants. However, the development of microvessels within the leaflet was
499 evident in the 12 months explants, with microvessels formed at the base and mid regions
500 of the leaflet. After 24 months, some microvessels were also present at the tip region of
501 the leaflet. Additionally, larger blood vessels were present within the neotissue layer over
502 the whole leaflet.

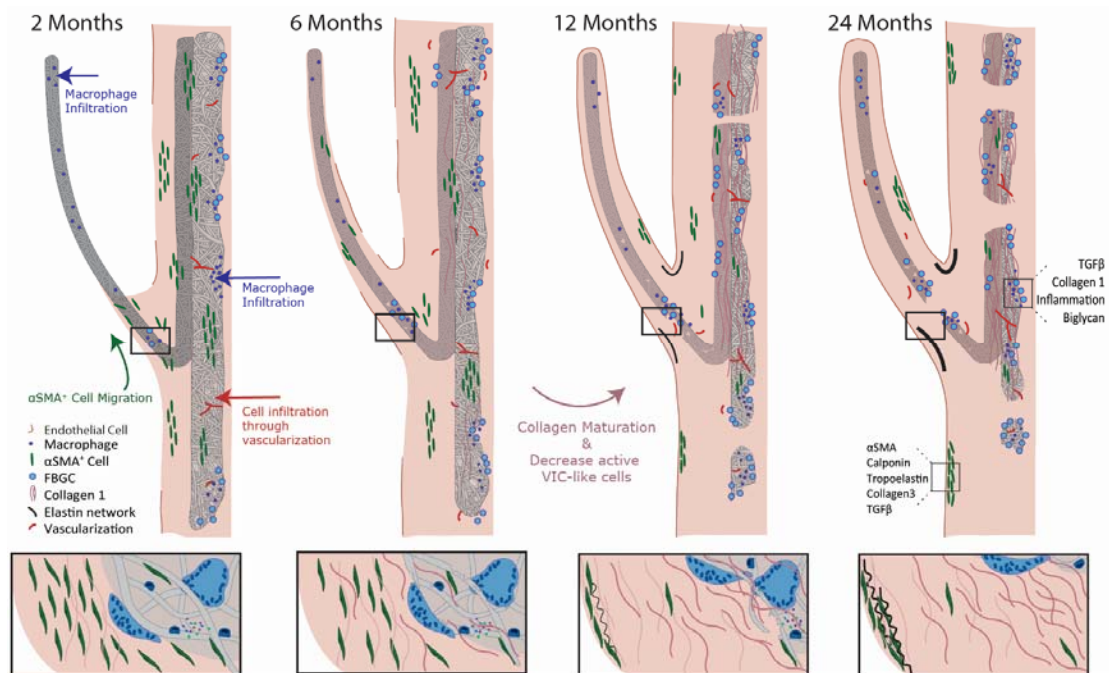
503

504 **Discussion**

505 Within this study we aimed to gain more insight into the long-term *in vivo* inflammatory
506 and regenerative processes in *in situ* TEHVs based on resorbable supramolecular
507 elastomers. Enabled by a combination of Raman microspectroscopy and IHC, the main

508 findings of this study are that: (1) inflammatory cells, and macrophages in particular,
509 infiltrated the grafts in all regions, with a heterogenous location-dependent phenotype; (2)
510 the resorption of the synthetic graft material was strongly location-dependent, with most
511 rapid resorption in the conduit and leaflet base regions, and correlated with the presence
512 of FBGCs; (3) collagen maturation was effectuated predominantly between 6 and 12
513 months of implantation, which coincided with a switch to a more quiescent VIC-like
514 phenotype; (4) microvessels formed throughout the microporous graft material, forming a
515 potential source for cell influx. Moreover, substantial valve-to-valve variability in the
516 spatiotemporal distribution of cells, tissue and graft resorption was detected, with most
517 pronounced variability noted in specimens following implantation of 6 and 12 months. A
518 schematic overview of the key findings is shown in **Figure 9**.

519



520

521 **Figure 9: Schematic overview of essential processes involved in *in situ* heart valve**
522 **regeneration.** After 2 months, macrophages had infiltrated the graft material of both the leaflet and
523 conduit. In the conduit, a microvasculature was already forming, providing an additional cell source.
524 αSMA⁺ cells migrated from the conduit towards the tip of the leaflet over time, depositing collagen
525 3-rich tissue. The deposited collagenous tissue became more mature through 6-12 months,
26

526 accompanied by a decrease in α SMA⁺ cells within this timeframe. Graft resorption was most
527 pronounced in the leaflet base and conduit correlating with a high presence of FBGCs in an
528 inflammatory environment, eventually causing successive resorption within these regions after 24
529 months. Inflammation had resolved in regions with complete graft resorption. Areas with ongoing
530 inflammation were high in TGF- β ₁, collagen 1 and biglycan. Areas in which α SMA⁺ cells localized
531 underneath the endothelium were high in calponin⁺ cells, (tropo)elastin, collagen 3 and TGF- β ₁.

532

533 Our data shed more light onto the processes of *in situ* heart valve tissue engineering. So
534 far, the knowledge on *in situ* heart valve tissue engineering using resorbable synthetic
535 scaffolds has been largely speculative and predominantly based on studies on *in situ*
536 tissue-engineered vascular grafts, which have a less complex geometry and
537 hemodynamic environment. Recent data for vascular grafts suggests that the regenerative
538 response is driven by inflammation[36]–[38]. Macrophages, in particular, are thought to be
539 instrumental cellular players in this process as they have a dual function: on the one hand,
540 macrophages govern tissue formation via cross-talk to tissue-producing cells [39]–[41],
541 while on the other hand, macrophages dictate graft resorption through oxidative and
542 enzymatic pathways [42][43]. Here, we observed an influx of macrophages throughout all
543 regions of the graft materials, suggesting indeed a dominant role for these cells in the
544 regenerative cascade. Moreover, scaffold resorption was highly localized and associated
545 with presence of FBGCs, suggesting a role for these fused macrophages in degrading the
546 synthetic graft material through eliciting reactive oxygen species (ROS) [44]. However, the
547 relative contributions of individual macrophages and FBGCs in graft resorption remain
548 unclear. Interestingly, the FBGC formation in the conduit region tended to localize around
549 the outer boundaries of the graft material, rather than within the pores of the highly porous
550 graft material as was observed in the leaflet material. This difference may be a
551 consequence of the differences in hemodynamics between the moving leaflet versus the
552 static conduit wall. Alternatively, subtle differences in microstructure, e.g. fiber diameter
553 and pore size, between leaflet material 1 and conduit material 2 may have played a role.

554 Pore size is one of the design parameters known to influence cell infiltration, fibroblast
555 activation as well as macrophage polarization [45]–[47]. Moreover, Wissing et al.
556 previously showed that resorption of microfibrinous scaffolds by macrophages is dependent
557 on the scaffold microstructure [48]. *In vitro* FBGC formation is known to be regulated by
558 multiple factors, such as cell density, material chemistry and structure, and interleukin-4
559 (IL-4) stimulation, with the latter being recently suggested to be most important [44], [49],
560 [50]. In the leaflet base and conduit regions more transmural migration of macrophages is
561 occurring and more M2 macrophages, known to secrete IL-4, are present alongside iNOS
562 positive macrophages, when compared to the mid and tip region of the leaflet. Possibly,
563 this contributes to a higher presence of FBGCs in the base and wall region.

564 Notably, the FBGC- and macrophage-rich regions were also the most active regions of
565 cell activation and tissue formation. These activated cells had phenotypic features in
566 common with VICs. Dependent on the mechanism of stimulation, macrophages undergo
567 phenotypic modulation and secrete a variety of paracrine factors by which they regulate
568 the behavior of tissue-producing cells (e.g. differentiation, migration and proliferation) and
569 thus the deposition of new extracellular matrix [39]–[41], [51]. Importantly, it was observed
570 that macrophages cleared from regions in which the scaffold had been completely
571 resorbed, thereby preventing a chronic inflammatory environment that may cause excess
572 collagenous-fibrous tissue deposition, eventually leading to valve stiffening and
573 malfunctioning [52]. The balance between graft resorption and neotissue formation is of
574 utmost importance in order to maintain the mechanical integrity of the valve during the
575 regenerative response, especially within the stringent hemodynamic environment, as
576 unbalanced remodeling could lead to early graft failure or cause prolonged inflammation
577 and accumulation of fibrotic tissue. The Raman microspectroscopy analysis uniquely
578 enabled the precise characterization of the molecular composition of both tissue and graft
579 material in the same locations. Interestingly, TCA analysis suggested the presence of
580 fibrin-like tissue, tightly surrounding the synthetic graft fibers, in both graft materials at all
581 timepoints (**Supplementary Figure S11**). Within these regions, erythrocytes and overlap

582 with blood components, could also be detected, both inside graft material and the
583 neotissue surrounding the graft material. It is interesting to further define this structure, as
584 fibrin is thought to be deposited as part of the early host response [53] and to serve as a
585 template for new tissue formation similar to the preliminary matrix in physiological wound
586 healing [54]. Importantly, we detected that collagen maturation developed mainly
587 between 6 and 12 months after implantation. The immunohistochemical stainings
588 revealed a transition from a more collagen 3 to a more collagen 1 dominated tissue, which
589 is similar to physiological wound healing.

590 The formation of elastic fibers was detected only at late timepoints, with mature elastic
591 fibers mainly detected after 24 months of implantation. In native heart valves, the elastin
592 network is formed at the very early life stages and remains functional throughout a
593 lifetime, with little to no new elastin formation [55]. Similar to previous studies, sparse
594 mature elastic fiber formation was detected, although not yet comparable to the native
595 elastic fiber network [18][56]. In all valves, (tropo)elastin was extensively produced,
596 whereas the expression of the microfibrillar network protein fibrillin 1 and fibrillin 2 was
597 very sparsely detected. This suggests that the bottleneck for new elastic fiber formation
598 might not be the production of tropoelastin and the formation of elastin as such, but rather
599 the presence and/or assembly of network proteins. We speculate that the abundant
600 presence of inflammatory cells leads to a proteolytic environment of elastases and matrix
601 metalloproteinases (MMPs) that may inhibit elastogenesis [57]. This may also explain why
602 elastic fiber assembly was only detected at late time points, at which the inflammatory
603 environment had locally resolved in graft-free regions. The latter was recently reported by
604 Duijvelshoff et al., who demonstrated a trend of mature elastic fiber regeneration in
605 resorbable synthetic endovascular stents in pace with a reduction in macrophage
606 presence [58]. Overall, the present findings regarding tissue formation and maturation
607 suggest that scaffold resorption of *in situ* TEHVs should be relatively slow in order to allow
608 for sufficient mature and functional tissue formation prior to full scaffold resorption.

609 Interestingly, the maturation of the tissue was accompanied by a switch in the phenotype
610 of the VIC-like cells to a more quiescent α SMA⁺ phenotype. In healthy adult valves mainly
611 quiescent VICs, marked by e.g. vimentin, reside within the leaflet [59], [60], with
612 subpopulations of smooth muscle cells and myofibroblasts [59], [61]. Surprisingly,
613 vimentin positive cells infiltrated only very sparsely in the explants, whereas in the native
614 sheep aortic valve used as positive control, many cells expressing vimentin were present.
615 It is unclear what is the cause of this lack of vimentin expression. Especially at early
616 timepoints, α SMA and calponin positive cells were abundantly present within the explants.
617 The presence of these activated fibroblasts is typically associated with pathological
618 remodeling and excess tissue deposition [62]. However, for *in situ* TE these cells are
619 essential to facilitate endogenous tissue deposition. We believe it is essential that over
620 time these cells return to their quiescent state to prevent fibrosis and leaflet contraction,
621 as previously seen in many *in vitro* tissue-engineered heart valves [63], [64]. The marked
622 decrease in the presence of α SMA and calponin positive cells over time, accompanied
623 with the maturation of the tissue and the resorption of the scaffolds, indeed suggests that
624 the regenerative response in the explants was moving towards a state of tissue
625 homeostasis, rather than pathological remodeling. However, longer follow-up times are
626 warranted to investigate the functionality and composition of the valves upon complete
627 resorption of the graft materials. It also should be considered that native sheep valves
628 have differences when compared to native human valves. Typically, ovine leaflets have a
629 higher cellularity, more defined valvular layers and a lower amount of elastin [26], [65].
630 Moreover, Dekker et al. recently demonstrated that native ovine valves display a higher
631 expression of activated VICs when compared to human valves [26]. Such differences
632 should be considered when translating results from the ovine model towards human
633 application.

634 The exact source and routes of cellular influx could not be identified from this
635 retrospective study, and are topic of active investigation. Rapid cellularization of the
636 leaflets of acellular valvular implants has been previously reported already 5h [66] and
30

637 15h [67] post-implantation, proposing that these cells originate from the blood.
638 Additionally, influx of cells through transmural migration from the surrounding tissue was
639 reported at later follow-up times [68]. Recent research suggests a dominant role of
640 transmural migration of the surrounding tissue in small-diameter vascular graft
641 regeneration [69]. Within the present study, after 2 months, macrophages, predominantly
642 of a pro-inflammatory phenotype, were present within the leaflet especially near the tip,
643 suggesting a likely origin from the circulation. Within the conduit, immune cell infiltration
644 occurred most probably through transmural migration and neovascularization.
645 Interestingly, calponin and SMemb positive cells were present within leaflet after 2
646 months, whereas α SMA⁺ cells were not found within the leaflet material but seemed to
647 migrate from the neotissue of the wall over the leaflet material with time. The exact origin
648 of the tissue producing cells remains unknown, however these results suggest that, similar
649 to the infiltrating immune cells, these cells originate from various sources and from various
650 precursor cells. In this respect, interesting phenomena were observed in the neotissue
651 layers near the lumen, with progressively more α SMA and calponin positive cells present
652 directly underneath the endothelium. This correlated with high levels of TGF- β and
653 biglycan and deposition of collagen 3, which could indicate endothelium-to-mesenchymal
654 transition (EndMT)[70], [71]. It is known that VEC-VIC interaction is very important for
655 valve homeostasis. In adult valves, limited EndMT is taking place, and this process can
656 contribute to replenish the VIC population as part of physiological valve remodeling [70].
657 However, an increased EndMT in adult valves is often associated with pathological
658 remodeling [72]. For the analyzed explants, it remains debatable whether the process of
659 EndMT is in fact ongoing, and if so, if it is leading to pathological remodeling or is simply
660 part of the necessary wound healing response for example as an additional source of
661 tissue producing cells.

662 One of the most important findings of this study is the spatial heterogeneity in cellular
663 phenotypes, tissue formation and scaffold resorption. While this may partly be explained
664 by the different sources of cell influx in the different regions, these spatial patterns also

665 suggest an important role for the heterogeneous local hemodynamic loads. Shear
666 stresses have been shown to play a dominant influence on the recruitment of monocytes
667 to electrospun scaffolds [73], [74]. In addition, both macrophages and tissue-producing
668 cells, such as (myo)fibroblasts and VICs, are known to be highly mechanosensitive [75],
669 [76]. *In vitro* studies have demonstrated cyclic strain to influence macrophage polarization
670 [77], [78]. Moreover, cyclic strain decreased degradative activity of macrophages within a
671 biomaterial [78]. Additionally, both cyclic stretch and shear stress influence the cross-talk
672 between (myo)fibroblasts and macrophages, and by that affecting tissue deposition [79].
673 Recent *in vivo* studies have shown the importance of hemodynamics in inflammation-
674 driven *in situ* tissue regeneration of vascular grafts [80]–[82] and valves [16]. Moreover, in
675 accordance with the present findings, Motta et al. recently reported on the importance of
676 hemodynamic loads, in particular cyclic stretch, on the inflammation and *in situ*
677 regeneration of de novo engineered extracellular matrix-based TEHVs [83]. In order to
678 enable better prediction of *in situ* (mal)adaptive remodeling, hypothesis-driven studies
679 have been focusing on macrophage and tissue-producing cell behavior and the influence
680 of their microenvironment such as graft design (e.g. porosity, surface chemistry), as well
681 as mechanical loading [16], [25], [46], [76], [79], [82], [84].

682 Finally, even within this very homologous test group of healthy, young sheep, variability
683 was seen between explants of each time point. Most variability in tissue formation, as well
684 as inflammation and graft resorption, between the valves tended to occur in the first 6
685 months. Within this timeframe, many processes are ongoing, influencing the timing and
686 extend of other processes involved in endogenous tissue regenerative cascade. Potential
687 sources of variability might be minor variabilities in the surgical procedure at implantation
688 or through differences in host immunological state [10]. Reasonably, more variation can
689 be expected when translating towards more heterogenous patient populations. Additional
690 sources of variability are proposed to include genetic variation, co-morbidities and sex-
691 and age-related changes, medications and environmental factors [10][85].

692 **Limitations**

693 This study has several limitations. One important limitation is that this was a retrospective
694 study and only endpoint data measurements were used in this study. Therefore, it remains
695 speculative which early events could have led to certain downstream remodeling. Spectral
696 analysis of Raman data was performed only within the graft material. As longitudinal
697 analysis of a single valve was not possible, variability between selected areas could occur
698 due to resorption of graft material, especially in the base region. Therefore, resorption in
699 this region seemed less pronounced when comparing Raman analysis and
700 immunohistochemical visualization. Additionally, intense signal and close material
701 interactions, such as fibrin, might cause noise in the spectrum. A more detailed pixel size
702 could be used to overcome this limitation, however, here we opted for compromising on
703 the minimal pixel size in order to enable scanning of various larger regions within the
704 valve. Another limitation of this study is the limited sample size. However, there are only
705 few studies on long-term *in vivo* implantations of resorbable synthetic heart valves
706 available to date, so despite the limited sample numbers, the presented information
707 represents a valuable contribution to our understanding of *in situ* heart valve tissue
708 engineering.

709 **Conclusion**

710 With these analyses, we uncovered new insights in the endogenous tissue restoration
711 response regarding infiltration and presence of immune cells and tissue forming cells and
712 their correlation to graft resorption and neotissue formation and maturation over time. Our
713 findings show important spatial heterogeneities in the regenerative process, most likely as
714 the combined effect of heterogeneous cellular repopulation mechanisms and
715 heterogeneity in the local hemodynamic loads, which may fuel the rational design of
716 improved grafts. To fully understand the *in situ* regenerative response, more in-depth,
717 comprehensive *in vivo* analysis and mechanistic *in vitro* work with focus on the role of
718 local hemodynamics and the downstream effects thereof are warranted. However, to

719 ensure robust clinical translation, a holistic approach is needed, focusing not only on the
720 graft properties, but also on implant-independent, patient-specific factors.

721

722 **CRedit author statement**

723 **Bente de Kort:** Investigation, Formal Analysis, Data curation, Visualization, Writing–
724 Original Draft; **Julia Marzi:** Investigation, Formal analysis, Visualization, Writing-Review &
725 Editing; **Eva Brauchle:** Investigation, Formal analysis; **Arturo Lichauco:** Software,
726 Validation; **Hannah Bauer:** Validation, Writing-Review & Editing; **Aurelie Serrero:**
727 Resources, Writing-Review & Editing; **Sylvia Dekker:** Resources, Validation; **Martijn**
728 **Cox:** Conceptualization, Resources, Writing-Review & Editing; **Fred Schoen:** Validation,
729 Writing-Review & Editing; **Katja Schenke-Layland:** Resources, Writing-Review & Editing;
730 **Carlijn Bouten:** Writing-Review & Editing, Funding acquisition; **Anthal Smits:**
731 Conceptualization, Formal Analysis, Writing–Original Draft & Editing, Funding acquisition,
732 Supervision.

733 **Competing interests statement**

734 The research labs from K. Schenke-Layland and A. Smits performed independent
735 scientific contract work for the company Xeltis and received for this work financial
736 compensation. M. Cox, H. Bauer and A. Serrero are employees of Xeltis, M. Cox and C.
737 Bouten are shareholders of Xeltis and F. Schoen is a financially compensated scientific
738 advisor to Xeltis. All other authors report no competing interests.

739 **Funding**

740 This research was financially supported by the Gravitation Program “Materials
741 Driven Regeneration”, funded by the Netherlands Organization for Scientific
742 Research (024.003.013), and a Career Acceleration and Development Grant to A.
743 Smits by the CardioVascular Research Netherlands (CVON) 1Valve consortium.
744 The collaboration between Eindhoven University of Technology and the University

745 of Tübingen for the Raman microspectroscopy analysis was facilitated by a Short-
746 Term Fellowship (8169) of the European Molecular Biology Organization (EMBO)
747 to A. Smits. This study was financially supported by the Ministry of Science, Research
748 and the Arts of Baden-Württemberg (33-729.55-3/214 and SI-BW 01222-91 to K.S.-L.)
749 and the Deutsche Forschungsgemeinschaft (INST 2388/64-1 to K.S.-L.).

750

751 **References**

- 752 [1] S. H. Rahimtoola, "Choice of Prosthetic Heart Valve in Adults. An Update," *J. Am.*
753 *Coll. Cardiol.*, vol. 55, no. 22, pp. 2413–2426, 2010.
- 754 [2] P. Bloomfield, D. J. Wheatley, R. J. Prescott, and H. C. Miller, "Twelve-year
755 comparison of a Bjork-Shiley mechanical heart valve with porcine bioprostheses,"
756 *N. Engl. J. Med.*, vol. 324, no. 9, pp. 573–9, 1991.
- 757 [3] K. Hammermeister, G. K. Sethi, W. G. Henderson, F. L. Grover, C. Oprian, and S.
758 H. Rahimtoola, "Outcomes 15 years after valve replacement with a mechanical
759 versus a bioprosthetic valve: Final report of the Veterans Affairs randomized trial,"
760 *J. Am. Coll. Cardiol.*, vol. 36, no. 4, pp. 1152–1158, 2000.
- 761 [4] T. Bourguignon *et al.*, "Very long-term outcomes of the carpentier-edwards
762 perimount valve in aortic position," *Ann. Thorac. Surg.*, vol. 99, no. 3, pp. 831–837,
763 2015.
- 764 [5] G. Costa, E. Criscione, D. Todaro, C. Tamburino, and M. Barbanti, "Long-term
765 transcatheter aortic valve durability," *Interv. Cardiol. Rev.*, vol. 14, no. 2, pp. 62–69,
766 2019.
- 767 [6] F. Sawaya, T. H. Jørgensen, L. Søndergaard, and O. De Backer, "Transcatheter
768 Bioprosthetic Aortic Valve Dysfunction: What We Know So Far," *Front. Cardiovasc.*
769 *Med.*, vol. 6, no. October, pp. 1–8, 2019.

- 770 [7] T. B. Wissing, V. Bonito, C. V. C. Bouten, and A. I. P. M. Smits, "Biomaterial-driven
771 in situ cardiovascular tissue engineering—a multi-disciplinary perspective," *npj*
772 *Regen. Med.*, vol. 2, no. 1, p. 18, Dec. 2017.
- 773 [8] C. V. C. Bouten, A. I. P. M. Smits, and F. P. T. Baaijens, "Can We Grow Valves
774 Inside the Heart? Perspective on Material-based In Situ Heart Valve Tissue
775 Engineering," *Front. Cardiovasc. Med.*, vol. 5, no. May, pp. 1–10, May 2018.
- 776 [9] E. S. Fioretta *et al.*, "Next-generation tissue-engineered heart valves with repair,
777 remodelling and regeneration capacity," *Nature Reviews Cardiology*, vol. 18, no. 2.
778 Springer US, pp. 92–116, 09-Feb-2021.
- 779 [10] A. I. P. M. Smits and C. V. C. Bouten, "Tissue engineering meets
780 immunoengineering: Prospective on personalized in situ tissue engineering
781 strategies," *Curr. Opin. Biomed. Eng.*, vol. 6, pp. 17–26, Jun. 2018.
- 782 [11] J. W. van Rijswijk *et al.*, "Failure of decellularized porcine small intestinal
783 submucosa as a heart valved conduit," *J. Thorac. Cardiovasc. Surg.*, vol. 160, no.
784 4, pp. e201–e215, Oct. 2020.
- 785 [12] T. Goecke *et al.*, "In vivo performance of freeze-dried decellularized pulmonary
786 heart valve allo- and xenografts orthotopically implanted into juvenile sheep," *Acta*
787 *Biomater.*, vol. 68, pp. 41–52, Mar. 2018.
- 788 [13] R. Ramm *et al.*, "Decellularization combined with enzymatic removal of N-linked
789 glycans and residual DNA reduces inflammatory response and improves
790 performance of porcine xenogeneic pulmonary heart valves in an ovine in vivo
791 model," *Xenotransplantation*, vol. 27, no. 2, pp. 1–12, Mar. 2020.
- 792 [14] S. E. Motta *et al.*, "Human cell-derived tissue-engineered heart valve with
793 integrated Valsalva sinuses: towards native-like transcatheter pulmonary valve
794 replacements," *npj Regen. Med.*, vol. 4, no. 1, p. 14, Dec. 2019.
- 795 [15] V. Lintas *et al.*, "Development of a Novel Human Cell-Derived Tissue-Engineered
36

- 796 Heart Valve for Transcatheter Aortic Valve Replacement: an In Vitro and In Vivo
797 Feasibility Study,” *J. Cardiovasc. Transl. Res.*, vol. 11, no. 6, pp. 470–482, 2018.
- 798 [16] M. Y. Emmert *et al.*, “Computational modeling guides tissue-engineered heart valve
799 design for long-term in vivo performance in a translational sheep model,” *Sci.*
800 *Transl. Med.*, vol. 10, no. 440, p. eaan4587, May 2018.
- 801 [17] J. Reimer, Z. Syedain, B. Haynie, M. Lahti, J. Berry, and R. Tranquillo,
802 “Implantation of a Tissue-Engineered Tubular Heart Valve in Growing Lambs,” *Ann.*
803 *Biomed. Eng.*, vol. 45, no. 2, pp. 439–451, Feb. 2017.
- 804 [18] J. Kluin *et al.*, “Biomaterials In situ heart valve tissue engineering using a
805 bioresorbable elastomeric implant e From material design to 12 months follow-up in
806 sheep,” *Biomaterials*, vol. 125, pp. 101–117, 2017.
- 807 [19] G. Bennink, S. Torii, M. Brugmans, and M. Cox, “A novel restorative pulmonary
808 valved conduit in a chronic sheep model□: Mid-term hemodynamic function and
809 histologic assessment,” *J. Thorac. Cardiovasc. Surg.*, 2017.
- 810 [20] Y. Miyazaki *et al.*, “Acute performance of a novel restorative transcatheter aortic
811 valve: Preclinical results,” *EuroIntervention*, vol. 13, no. 12, pp. e1410–e1417,
812 2017.
- 813 [21] G. N. Coyan, A. D. Amore, and Y. Matsumura, “In vivo functional assessment of a
814 novel degradable metal and elastomeric scaffold-based tissue engineered heart
815 valve,” *J. Thorac. Cardiovasc. Surg.*, 2018.
- 816 [22] D. L. Morales *et al.*, “A Novel Restorative Pulmonary Valve Conduit: Early
817 Outcomes of Two Clinical Trials,” *Front. Cardiovasc. Med.*, vol. 7, no. March, pp. 1–
818 9, Mar. 2021.
- 819 [23] R. Duijvelshoff *et al.*, “Inconsistency in Graft Outcome of Bilayered Bioresorbable
820 Supramolecular Arterial Scaffolds in Rats,” *Tissue Eng. Part A*, vol. 31, no. 0, p.
821 ten.tea.2020.0185, Oct. 2020.

- 822 [24] E. S. Fioretta *et al.*, “Differential Leaflet Remodeling of Bone Marrow Cell Pre-
823 Seeded Versus Nonseeded Bioresorbable Transcatheter Pulmonary Valve
824 Replacements,” *JACC Basic to Transl. Sci.*, vol. 5, no. 1, pp. 15–31, Jan. 2020.
- 825 [25] M. Uiterwijk *et al.*, “In Situ Remodeling Overrides Bioinspired Scaffold Architecture
826 of Supramolecular Elastomeric Tissue-Engineered Heart Valves,” *JACC Basic to
827 Transl. Sci.*, vol. 5, no. 12, pp. 1187–1206, Dec. 2020.
- 828 [26] S. Dekker, D. van Geemen, A. J. van den Bogaardt, A. Driessen-Mol, E. Aikawa,
829 and A. I. P. M. Smits, “Sheep-Specific Immunohistochemical Panel for the
830 Evaluation of Regenerative and Inflammatory Processes in Tissue-Engineered
831 Heart Valves,” *Front. Cardiovasc. Med.*, vol. 5, no. August, pp. 1–19, Aug. 2018.
- 832 [27] E. Brauchle and K. Schenke-Layland, “Raman spectroscopy in biomedicine - non-
833 invasive in vitro analysis of cells and extracellular matrix components in tissues,”
834 *Biotechnol. J.*, vol. 8, no. 3, pp. 288–297, 2013.
- 835 [28] J. Marzi, E. M. Brauchle, K. Schenke-Layland, and M. W. Rolle, “Non-invasive
836 functional molecular phenotyping of human smooth muscle cells utilized in
837 cardiovascular tissue engineering,” *Acta Biomater.*, vol. 89, pp. 193–205, 2019.
- 838 [29] Z. Movasaghi, S. Rehman, and I. U. Rehman, “Raman spectroscopy of biological
839 tissues,” *Appl. Spectrosc. Rev.*, vol. 42, no. 5, pp. 493–541, 2007.
- 840 [30] S. Hinderer, E. Brauchle, and K. Schenke-Layland, “Generation and Assessment of
841 Functional Biomaterial Scaffolds for Applications in Cardiovascular Tissue
842 Engineering and Regenerative Medicine,” *Adv. Healthc. Mater.*, vol. 4, no. 16, pp.
843 2326–2341, Nov. 2015.
- 844 [31] P. Bankhead *et al.*, “QuPath: Open source software for digital pathology image
845 analysis,” *Sci. Rep.*, vol. 7, no. 1, pp. 1–7, 2017.
- 846 [32] A. Zbinden *et al.*, “Non-invasive marker-independent high content analysis of a
847 microphysiological human pancreas-on-a-chip model,” *Matrix Biol.*, vol. 85–86, pp.

- 848 205–220, Jan. 2020.
- 849 [33] A. Zbinden *et al.*, “Nidogen-1 Mitigates Ischemia and Promotes Tissue Survival and
850 Regeneration,” *Adv. Sci.*, vol. 8, no. 4, p. 2002500, Feb. 2021.
- 851 [34] C. L. Jenkins, L. E. Bretscher, I. A. Guzei, and R. T. Raines, “Effect of 3-
852 hydroxyproline residues on collagen stability,” *J. Am. Chem. Soc.*, vol. 125, no. 21,
853 pp. 6422–6427, 2003.
- 854 [35] G. Pezzotti *et al.*, “Raman spectroscopy of human skin: looking for a quantitative
855 algorithm to reliably estimate human age,” *J. Biomed. Opt.*, vol. 20, no. 6, p.
856 065008, 2015.
- 857 [36] H. Talacua *et al.*, “*In Situ* Tissue Engineering of Functional Small-Diameter Blood
858 Vessels by Host Circulating Cells Only,” *Tissue Eng. Part A*, vol. 21, no. 19–20, pp.
859 2583–2594, 2015.
- 860 [37] N. Hibino *et al.*, “The innate immune system contributes to tissue-engineered
861 vascular graft performance,” *FASEB J.*, vol. 29, no. 6, pp. 2431–2438, Jun. 2015.
- 862 [38] M. Brugmans, A. Serrero, M. Cox, O. Svanidze, and F. J. Schoen, “Morphology and
863 mechanisms of a novel absorbable polymeric conduit in the pulmonary circulation
864 of sheep,” *Cardiovasc. Pathol.*, vol. 38, pp. 31–38, Jan. 2019.
- 865 [39] K. G. Battiston, R. S. Labow, C. A. Simmons, and J. P. Santerre,
866 “Immunomodulatory polymeric scaffold enhances extracellular matrix production in
867 cell co-cultures under dynamic mechanical stimulation,” *Acta Biomater.*, vol. 24, pp.
868 74–86, 2015.
- 869 [40] K. G. Battiston, B. Ouyang, R. S. Labow, C. A. Simmons, and J. P. Santerre,
870 “Monocyte/macrophage cytokine activity regulates vascular smooth muscle cell
871 function within a degradable polyurethane scaffold,” *Acta Biomater.*, vol. 10, no. 3,
872 pp. 1146–1155, 2014.

- 873 [41] D. T. Ploeger, N. A. Hosper, M. Schipper, J. A. Koerts, S. de Rond, and R. A. Bank,
874 “Cell plasticity in wound healing: paracrine factors of M1/ M2 polarized
875 macrophages influence the phenotypical state of dermal fibroblasts,” *Cell Commun.*
876 *Signal.*, vol. 11, no. 1, p. 29, 2013.
- 877 [42] M. C. P. Brugmans *et al.*, “Hydrolytic and oxidative degradation of electrospun
878 supramolecular biomaterials: In vitro degradation pathways,” *Acta Biomater.*, vol.
879 27, pp. 21–31, 2015.
- 880 [43] J. E. McBane, J. P. Santerre, and R. S. Labow, “The interaction between hydrolytic
881 and oxidative pathways in macrophage-mediated polyurethane degradation,” *J.*
882 *Biomed. Mater. Res. Part A*, vol. 82A, no. 4, pp. 984–994, Sep. 2007.
- 883 [44] R. Klopffleisch and F. Jung, “The pathology of the foreign body reaction against
884 biomaterials,” *J. Biomed. Mater. Res. - Part A*, vol. 105, no. 3, pp. 927–940, 2017.
- 885 [45] Y. Matsuzaki *et al.*, “The effect of pore diameter on neo-tissue formation in
886 electrospun biodegradable tissue-engineered arterial grafts in a large animal
887 model,” *Acta Biomater.*, vol. 115, pp. 176–184, 2020.
- 888 [46] S. Jiang *et al.*, “Cryoprotectant enables structural control of porous scaffolds for
889 exploration of cellular mechano-responsiveness in 3D,” *Nat. Commun.*, vol. 10, no.
890 1, 2019.
- 891 [47] D. G. Han *et al.*, “Optimization of electrospun poly(caprolactone) fiber diameter for
892 vascular scaffolds to maximize smooth muscle cell infiltration and phenotype
893 modulation,” *Polymers (Basel)*, vol. 11, no. 4, p. 643, Apr. 2019.
- 894 [48] T. B. Wissing *et al.*, “Macrophage-Driven Biomaterial Degradation Depends on
895 Scaffold Microarchitecture,” *Front. Bioeng. Biotechnol.*, vol. 7, no. APR, Apr. 2019.
- 896 [49] K. L. Trout and A. Holian, “Factors influencing multinucleated giant cell formation in
897 vitro,” *Immunobiology*, vol. 224, no. 6, pp. 834–842, 2019.

- 898 [50] A. K. McNally and J. M. Anderson, "Phenotypic expression in human monocyte-
899 derived interleukin-4-induced foreign body giant cells and macrophages in vitro □:
900 Dependence on material surface properties," *J. Biomed. Mater. Res. Part A*, vol.
901 103, no. 4, pp. 1380–1390, Apr. 2015.
- 902 [51] E. Song, N. Ouyang, M. Hörbelt, B. Antus, M. Wang, and M. S. Exton, "Influence of
903 alternatively and classically activated macrophages on fibrogenic activities of
904 human fibroblasts," *Cell. Immunol.*, vol. 204, no. 1, pp. 19–28, 2000.
- 905 [52] G. J. Mahler and J. T. Butcher, "Inflammatory Regulation of Valvular Remodeling:
906 The Good(?), the Bad, and the Ugly," *Int. J. Inflam.*, vol. 2011, pp. 1–13, 2011.
- 907 [53] J. W. Reinhardt *et al.*, "Early natural history of neotissue formation in tissue-
908 engineered vascular grafts in a murine model," *Regen. Med.*, vol. 14, no. 5, pp.
909 389–408, May 2019.
- 910 [54] N. Laurens, P. Koolwijk, and P. M. De Maat, "Fibrin structure and wound healing,"
911 *J. Thromb. Haemost.*, no. 4, pp. 932–939, 2006.
- 912 [55] M. Votteler *et al.*, "Elastogenesis at the onset of human cardiac valve
913 development," *Development*, vol. 140, no. 11, pp. 2345–2353, Jun. 2013.
- 914 [56] S. E. Motta *et al.*, "Development of an Off-the-Shelf Tissue-Engineered Sinus Valve
915 for Transcatheter Pulmonary Valve Replacement: a Proof-of-Concept Study," *J.*
916 *Cardiovasc. Transl. Res.*, vol. 11, no. 3, pp. 182–191, Jun. 2018.
- 917 [57] J. L. Ashworth *et al.*, "Fibrillin degradation by matrix metalloproteinases:
918 Implications for connective tissue remodelling," *Biochem. J.*, vol. 340, no. 1, pp.
919 171–181, 1999.
- 920 [58] R. Duijvelshoff *et al.*, "Transcatheter-Delivered Expandable Bioresorbable
921 Polymeric Graft With Stenting Capacity Induces Vascular Regeneration," *JACC*
922 *Basic to Transl. Sci.*, vol. 5, no. 11, pp. 1095–1110, Nov. 2020.

- 923 [59] E. Aikawa *et al.*, “Human semilunar cardiac valve remodeling by activated cells
924 from fetus to adult: Implications for postnatal adaptation, pathology, and tissue
925 engineering,” *Circulation*, vol. 113, no. 10, pp. 1344–1352, 2006.
- 926 [60] E. Rabkin-Aikawa *et al.*, “Clinical pulmonary autograft valves: Pathologic evidence
927 of adaptive remodeling in the aortic site,” *J. Thorac. Cardiovasc. Surg.*, 2004.
- 928 [61] K. Schenke-Layland, I. Riemann, F. Opitz, K. König, K. J. Halhuber, and U. A.
929 Stock, “Comparative study of cellular and extracellular matrix composition of native
930 and tissue engineered heart valves,” *Matrix Biol.*, vol. 23, no. 2, pp. 113–125, 2004.
- 931 [62] A. C. Liu, V. R. Joag, and A. I. Gotlieb, “The Emerging Role of Valve Interstitial Cell
932 Phenotypes in Regulating Heart Valve Pathobiology,” *Am. J. Pathol.*, vol. 171, no.
933 5, pp. 1407–1418, Nov. 2007.
- 934 [63] Z. H. Syedain *et al.*, “Implantation of a Tissue-engineered Heart Valve from Human
935 Fibroblasts Exhibiting Short Term Function in the Sheep Pulmonary Artery,”
936 *Cardiovasc. Eng. Technol.*, vol. 2, no. 2, pp. 101–112, Jun. 2011.
- 937 [64] T. C. Flanagan *et al.*, “In vivo remodeling and structural characterization of fibrin-
938 based tissue-engineered heart valves in the adult sheep model,” *Tissue Eng. - Part*
939 *A*, vol. 15, no. 10, pp. 2965–2976, 2009.
- 940 [65] D. van Geemen *et al.*, “Variation in tissue outcome of ovine and human engineered
941 heart valve constructs: relevance for tissue engineering,” pp. 59–70.
- 942 [66] A. Driessen-Mol *et al.*, “Transcatheter implantation of homologous ‘off-the-shelf’
943 tissue-engineered heart valves with self-repair capacity: Long-term functionality and
944 rapid in vivo remodeling in sheep,” *J. Am. Coll. Cardiol.*, vol. 63, no. 13, pp. 1320–
945 1329, 2014.
- 946 [67] A. K. Capulli *et al.*, “JetValve: Rapid manufacturing of biohybrid scaffolds for
947 biomimetic heart valve replacement,” *Biomaterials*, vol. 133, pp. 229–241, Jul.
948 2017.

- 949 [68] Z. Syedain *et al.*, “6-Month aortic valve implantation of an off-the-shelf tissue-
950 engineered valve in sheep,” *Biomaterials*, vol. 73, pp. 175–184, Dec. 2015.
- 951 [69] J. Liu *et al.*, “The surrounding tissue contributes to smooth muscle cells’
952 regeneration and vascularization of small diameter vascular grafts,” *Biomater. Sci.*,
953 vol. 7, no. 3, pp. 914–925, Feb. 2019.
- 954 [70] D. E. P. Muylaert *et al.*, “Environmental Influences on Endothelial to Mesenchymal
955 Transition in Developing Implanted Cardiovascular Tissue-Engineered Grafts,”
956 *Tissue Eng. Part B Rev.*, vol. 22, no. 1, pp. 58–67, Feb. 2016.
- 957 [71] Y. Akatsu *et al.*, “Fibroblast growth factor signals regulate transforming growth
958 factor- β -induced endothelial-to-myofibroblast transition of tumor endothelial cells
959 via Elk1,” *Mol. Oncol.*, vol. 13, no. 8, pp. 1706–1724, 2019.
- 960 [72] S. Piera-Velazquez and S. A. Jimenez, “Endothelial to Mesenchymal Transition:
961 Role in Physiology and in the Pathogenesis of Human Diseases,” *Physiol. Rev.*,
962 vol. 99, no. 2, pp. 1281–1324, Apr. 2019.
- 963 [73] A. I. P. M. Smits, A. Driessen-Mol, C. V. C. Bouten, and F. P. T. Baaijens, “A
964 Mesofluidics-Based Test Platform for Systematic Development of Scaffolds for In
965 Situ Cardiovascular Tissue Engineering,” *Tissue Eng. Part C Methods*, vol. 18, no.
966 6, pp. 475–485, Jun. 2012.
- 967 [74] A. I. P. M. Smits, V. Ballotta, A. Driessen-Mol, C. V. C. Bouten, and F. P. T.
968 Baaijens, “Shear flow affects selective monocyte recruitment into <sc>MCP</sc>
969 -1-loaded scaffolds,” *J. Cell. Mol. Med.*, vol. 18, no. 11, pp. 2176–2188, Nov. 2014.
- 970 [75] C. A. Carruthers, C. M. Alfieri, E. M. Joyce, S. C. Watkins, K. E. Yutzey, and M. S.
971 Sacks, “Gene Expression and Collagen Fiber Micromechanical Interactions of the
972 Semilunar Heart Valve Interstitial Cell,” *Cell. Mol. Bioeng.*, vol. 5, no. 3, pp. 254–
973 265, Sep. 2012.

- 974 [76] P. Thayer *et al.*, “The effects of combined cyclic stretch and pressure on the aortic
975 valve interstitial cell phenotype,” *Ann. Biomed. Eng.*, vol. 39, no. 6, pp. 1654–1667,
976 2011.
- 977 [77] V. Bonito, B. J. de Kort, C. V. C. Bouten, and A. I. P. M. Smits, “Cyclic Strain
978 Affects Macrophage Cytokine Secretion and Extracellular Matrix Turnover in
979 Electrospun Scaffolds,” *Tissue Eng. Part A*, vol. 25, no. 17–18, pp. 1310–1325,
980 Sep. 2019.
- 981 [78] T. B. Wissing *et al.*, “Hemodynamic loads distinctively impact the secretory profile
982 of biomaterial-activated macrophages-implications for in situ vascular tissue
983 engineering,” *Biomater. Sci.*, vol. 8, no. 1, pp. 132–147, 2020.
- 984 [79] E. E. Haaften, T. B. Wissing, N. A. Kurniawan, A. I. P. M. Smits, and C. V. C.
985 Bouten, “Human In Vitro Model Mimicking Material-Driven Vascular Regeneration
986 Reveals How Cyclic Stretch and Shear Stress Differentially Modulate Inflammation
987 and Matrix Deposition,” *Adv. Biosyst.*, vol. 4, no. 6, p. 1900249, Jun. 2020.
- 988 [80] C. A. Best *et al.*, “Differential outcomes of venous and arterial tissue engineered
989 vascular grafts highlight the importance of coupling long-term implantation studies
990 with computational modeling,” *Acta Biomater.*, vol. 94, pp. 183–194, Aug. 2019.
- 991 [81] R. Khosravi, A. B. Ramachandra, J. M. Szafron, D. E. Schiavazzi, C. K. Breuer, and
992 J. D. Humphrey, “A computational bio-chemo-mechanical model of in vivo tissue-
993 engineered vascular graft development,” *Integr. Biol.*, vol. 12, no. 3, pp. 47–63, Apr.
994 2020.
- 995 [82] Y.-L. Wu *et al.*, “Electrospun Tissue-Engineered Arterial Graft Thickness Affects
996 Long-Term Composition and Mechanics,” *Tissue Eng. Part A*, vol. 00, no. 00, pp.
997 1–11, 2020.
- 998 [83] S. E. Motta *et al.*, “Geometry influences inflammatory host cell response and
999 remodeling in tissue-engineered heart valves in-vivo,” *Sci. Rep.*, vol. 10, no. 1, p.

1000 19882, Dec. 2020.

1001 [84] E. E. van Haaften *et al.*, “Decoupling the Effect of Shear Stress and Stretch on
1002 Tissue Growth and Remodeling in a Vascular Graft,” *Tissue Eng. Part C Methods*,
1003 vol. 24, no. 7, pp. 418–429, Jul. 2018.

1004 [85] B. L. Zhang, R. W. Bianco, and F. J. Schoen, “Preclinical Assessment of Cardiac
1005 Valve Substitutes: Current Status and Considerations for Engineered Tissue Heart
1006 Valves,” *Front. Cardiovasc. Med.*, vol. 6, no. June, pp. 1–9, Jun. 2019.

1007